Eikonal tomography: surface wave tomography by phase front tracking across a regional broad-band seismic array

Fan-Chi Lin,[1] Michael H. Ritzwoller[1] and Roel Snieder[2]

[1]*Center for Imaging the Earth's Interior, Department of Physics, University of Colorado at Boulder, Boulder,* CO 80309-0390, *USA.*
E-mail: fanchi.lin@colorado.edu
[2]*Center for Wave Phenomena and Department of Geophysics, Colorado School of Mines, Golden,* CO 80401, *USA*

SUMMARY

We present a new method of surface wave tomography based on applying the eikonal equation to observed phase traveltime surfaces computed from seismic ambient noise. The source–receiver reciprocity in the ambient noise method implies that each station can be considered to be an effective source and the phase traveltime between that source and all other stations is used to track the phase front and construct the phase traveltime surface. Assuming that the amplitude of the waveform varies smoothly, the eikonal equation states that the gradient of the phase traveltime surface can be used to estimate both the local phase speed and the direction of wave propagation. For each location, we statistically summarize the distribution of azimuthally dependent phase speed measurements based on the phase traveltime surfaces centred on different effective source locations to estimate both the isotropic and azimuthally anisotropic phase speeds and their uncertainties. Examples are presented for the 12 and 24 s Rayleigh waves for the EarthScope/USArray Transportable Array stations in the western USA. We show that (1) the major resulting tomographic features are consistent with traditional inversion methods, (2) reliable uncertainties can be estimated for both the isotropic and anisotropic phase speeds, (3) 'resolution' can be approximated by the coherence length of the phase speed measurements and is about equal to the station spacing, (4) no explicit regularization is required in the inversion process and (5) azimuthally dependent phase speed anisotropy can be observed directly without assuming its functional form.

Key words: Tomography; Surface waves and free oscillations; Seismic anisotropy; Wave propagation; North America.

1 INTRODUCTION

The seismic surface wave tomography inverse problem is normally approached in one of two ways that can be thought of as either 'single-station' or 'array-based' methods. Both methods have proven effective at revealing the spatial variability of surface wave speeds from global to regional scales.

The first (single-station) approach to surface wave tomography is based on traveltime measurements between a set of seismic sources (typically earthquakes) and a set of receivers (one receiver at a time). The traveltimes are then interpreted in terms of wave speeds in the medium of propagation using ray theory with straight or potentially bent rays (e.g. Trampert & Woodhouse 1996; Ekstrom *et al.* 1997; Ritzwoller & Levshin 1998; Yoshizawa & Kennett 2002) or finite frequency kernels (e.g. Dahlen *et al.* 2000; Ritzwoller *et al.* 2002; Levshin *et al.* 2005). This method results in a set of frequency-dependent dispersion maps of either Rayleigh or Love wave group or phase speed. This approach has also been applied to ambient noise data (e.g. Sabra *et al.* 2005; Shapiro *et al.* 2005; Yao *et al.* 2006; Moschetti *et al.* 2007; Lin *et al.* 2007; Yang *et al.* 2007;

Bensen *et al.* 2008), which provides wave traveltimes between pairs of receivers. In this case, one station can be considered to be an 'effective' source, but it is equivalent to the earthquake tomography problem in which the sources excite the wavefield. A variant of this method involves waveform fitting that in some cases bypasses the dispersion maps to construct the 3-D variation of shear wave speed directly in earth's interior (e.g. Woodhouse & Dziewonski 1984; Nolet 1990; van der Lee & Fredriksen 2005).

The second approach to surface wave tomography deals with stations as components of an array and interprets the phase difference observed between waves recorded across the array in terms of the dispersion characteristics of the medium. In doing so, this method either applies geometrical constraints on the stations, typically that they lie nearly along a great circle with the earthquake (e.g. Brisbourne & Stuart 1998; Prindle & Tanimoto 2006), or inverts for the characteristics of the incoming wave front along with the surface wave dispersion characteristics of the medium lying within the array (e.g. Alsina *et al.* 1993; Friederich 1998; Yang & Forsyth 2006).

In both approaches, the surface wave dispersion maps result from a regularized inverse problem that is typically solved by matrix
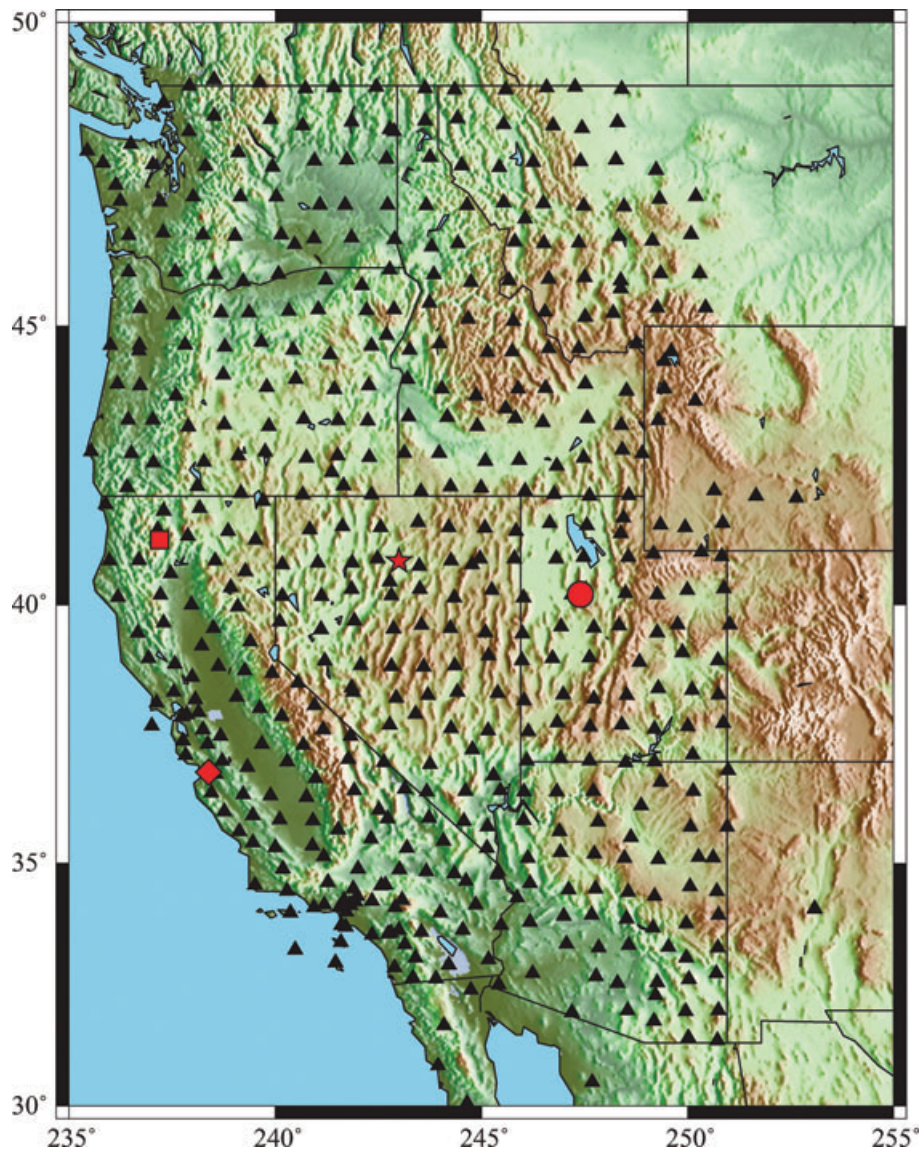
Figure 1. The 499 stations used in this study are identified by black triangles. Waveforms are taken continuously between October 2004 and November 2007. Most stations are from the EarthScope/USArray Transportable Array (TA), but a few exceptions exist, such as NARS Array stations in Mexico. The four red symbols identify locations used later in the paper.

inversion. Regularization in most cases is *ad hoc*, and includes spatial smoothing as well as matrix damping. As in many geophysical inverse problems, a trade-off between the amplitude of the heterogeneity and the resolution emerges that affects confidence in the smaller structural scales when high resolution is desired. This trade-off is most severe for azimuthal anisotropy, as has been well documented by previous studies (e.g. Laske & Master 1998; Levshin *et al.* 2001; Trampert & Woodhouse 2003; Smith *et al.* 2004; Deschamps *et al.* 2008), in which the amplitude of anisotropy is particularly poorly determined. These problems are exacerbated by the fact that uncertainty information that emerges for the maps tends to be unreliable. Theoretical approximations made in the inversion, such as the assumption of straight (great-circle) rays or approximate sensitivity kernels, also affect the quality of the resulting maps. This particularly calls into question the robustness of information about azimuthal anisotropy because the magnitude of the traveltime effects of azimuthal anisotropy and ray bending, for example, is similar.

The purpose of this paper is to present a new method of surface wave tomography that complements the traditional methods. The method is based on tracking surface wave fronts across an array of seismometers (Pollitz 2008) and should, therefore, be seen to lie within the tradition of array-based methods, although as will be seen in the discussion below the method degenerates to phase measurements obtained at single stations. The method is applicable, in principle, to surface waves generated both by earthquakes and ambient noise, but applications in this paper will concentrate on ambient noise recordings across the transportable array (TA) component of EarthScope/USArray (Fig. 1). Because it is an array-based method, however, an array is needed. The TA provides an ideal setting, but large PASSCAL experiments are suitable for the method and the emergence of large-scale arrays in Europe and China that mimic the station spacing of the TA also provide nearly optimal targets.

The method described in this paper is performed in three steps. We discuss the method here in the context of ambient noise tomography such that each station can be considered to be an effective

source as well as a receiver. The relevance of the method to earthquake tomography is discussed later in the paper. In the first step, a phase delay (or traveltime) surface is computed across the array centred on each station. We refer to this step as wave front or phase front tracking. In the second step, the gradient of each traveltime surface is computed at each spatial node. Invoking the eikonal equation, the magnitude of the gradient approximates local phase slowness and the direction of the gradient is the direction of propagation of the geometrical ray. Steps 1 and 2 are performed with every station in the array as the effective source for the traveltime surface. Finally, in step 3, for each spatial node the local phase speeds and wave path directions are compiled and averaged from the traveltime surfaces centred on each individual station in the array. Because step 2 invokes the Eikonal equation, we refer to the method as 'Eikonal tomography'.

Eikonal tomography complements traditional surface wave tomography in several ways. First, there is no explicit regularization and, hence, the method is largely free from *ad hoc* choices. The method as we implement it does, however, involve smoothing in tracking the phase fronts. Second, the method accounts for bent rays, but ray tracing is not needed. The gradient of the phase front provides information about the local direction of travel of the wave. The use of bent rays in traditional tomography would necessitate iteration with ray tracing performed on each iteration. Third, the method naturally generates error estimates for the resulting phase speed maps. In our opinion, this is more useful than relying on global misfit obtained by traditional inversion methods. Fourth, in the context of estimating azimuthal anisotropy, eikonal tomography directly measures azimuth-dependent phase velocities at each node. Unlike the traditional tomographic method, no *ad hoc* assumption about the functional dependence of the phase velocity with azimuth is made. Finally, in the construction of phase speed maps, the ray tracing and matrix construction and inversion of the traditional methods have been replaced by surface fitting, computation of gradients and averaging. The method, therefore, is computationally very fast and parallelizes trivially.

Although we have applied Eikonal tomography successfully from 8 s to 40 s period across the western USA, we present results here only for the 12 s and 24 s Rayleigh waves. In principle, the same method can be applied to Love waves as well. The results shown in this study are presented to illustrate the method. Interpretation of the results will be the subject of future contributions.

2 THEORETICAL PRELIMINARIES

The traditional approach to seismic tomography begins with a statement of the forward problem that links unknown earth functionals (such as seismic wave speeds, surface wave phase or group speeds, etc.) with observations. In surface wave tomography, when mode coupling and the directionality of scattering are neglected, this involves the computation of traveltimes from the 2-D distribution of (frequency dependent) surface wave phase speeds, $c(r)$, that can be written in integral form as

$$t(\boldsymbol{r}_s, \boldsymbol{r}_r) = \int A(\boldsymbol{r}, \boldsymbol{r}_s, \boldsymbol{r}_r) \frac{dx^m}{c(\boldsymbol{r})} \qquad (1)$$

where $\boldsymbol{r}_s$ and $\boldsymbol{r}_r$ are the source and receiver locations, $\boldsymbol{r}$ is an arbitrary point in the medium and $m = 1$ or 2 denotes line and area integrals, respectively. For 'ray theories', $m = 1$ and the integral kernel, $A(\boldsymbol{r}, \boldsymbol{r}_s, \boldsymbol{r}_r)$, vanishes except along the path, which is typically either a great-circle (straight ray) or a path determined by the spatial distribution of phase speed (geometrical ray theory), which

is known only approximately. Ray theories are fully accurate at infinite frequency and approximate at any finite frequency. For $m = 2$, the integral is over area, and the integral kernel represents the finite frequency spatial extent of structural sensitivity. The sensitivity kernel may be *ad hoc* (e.g. Gaussian beam) or determined from a scattering theory (e.g. Born/Rytov) given a particular 1-D or higher dimensional input model. Spatially extended kernels are referred to as finite frequency kernels, to contrast them with ray theories. Much of recent theoretical work in surface wave seismology has been devoted to developing increasingly sophisticated, and presumably accurate, representations of the integral kernel in eq. (1) (e.g. Zhou *et al.* 2004; Tromp *et al.* 2005), although debate continues about whether approximate finite frequency kernels are preferable practically to ray theories based on bent rays with *ad hoc* cross-sections (e.g. Yoshizawa & Kennett 2002; van der Hilst & de Hoop 2005; Montelli *et al.* 2006; Trampert & Spetzler 2006).

Eq. (1) defines traveltime as a 'global' constraint on structure; that is, it is a variable that depends on the unknown structure over an extended region of model space and is defined to be contrasted with 'local' constraints. The traditional primacy of the forward problem in defining the inverse problem necessitates that the inverse problem is similarly global in character. Traveltime observations constrain phase speeds non-locally, that is over an extended region of model space.

In contrast, eikonal tomography places the inverse problem in the primary role once the phase traveltime surfaces, $\tau(\boldsymbol{r}_i, \boldsymbol{r})$, for positions $\boldsymbol{r}$ relative to an effective source located at $\boldsymbol{r}_i$ are known. The Eikonal equation (e.g. Wielandt 1993; Shearer 1999) is based on the following:

$$\frac{1}{c_i(\boldsymbol{r})^2} = |\nabla \tau(\boldsymbol{r}_i, \boldsymbol{r})|^2 - \frac{\nabla^2 A_i(\boldsymbol{r})}{A_i(\boldsymbol{r})\omega^2}, \qquad (2)$$

which is derived directly from the Helmholtz equation. When the second term on the right-hand side is small, then

$$\frac{\hat{k}_i}{c_i(\boldsymbol{r})} \cong \nabla \tau(\boldsymbol{r}_i, \boldsymbol{r}). \qquad (3)$$

Here, c_i is the phase speed for traveltime surface i at position $\boldsymbol{r}$, ω is the frequency and A is the amplitude of an elastic wave at position $\boldsymbol{r}$. The gradient is computed relative to the field vector $\boldsymbol{r}$ and $\hat{k}_i$ is the unit wave number vector for the traveltime surface i at position $\boldsymbol{r}$. The eikonal equation, eq. (3), derives by ignoring the second term on the right-hand side in eq. (2). In this case, the magnitude of the gradient of the phase traveltime is simply related to the 'local' phase slowness at $\boldsymbol{r}$ and the direction of the gradient provides the 'local' direction of propagation of the wave. Thus, the eikonal equation places local constraints on the surface wave speed.

Dropping the second term on the right-hand side of eq. (2) is justified either at high frequencies or if the spatial variation of the amplitude field is small compared with the gradient of the traveltime surface. The latter is the less restrictive constraint and will hold if lateral phase speed variations are sufficiently smooth to produce a relatively smooth amplitude field. Moreover, when repeated measurements are performed with phase traveltime surfaces from different effective sources, the errors caused by dropping the amplitude term are likely to interfere destructively, but will contribute to the estimated uncertainty especially when the wavelength is shorter than the length scale of the velocity structure (Bodin & Maupin 2008). We take this interpretation as the basis for the use of the Eikonal equation and use synthetic tests, presented in Section 5.1, to confirm that the effect of dropping the amplitude term is not a significant source of error in this study. In addition, in

ambient noise tomography, absolute amplitude information is typically lost due to time- and frequency-domain normalization prior to cross-correlation (Bensen *et al.* 2007). In this circumstance, the computation of the second term on the right-hand side of eq. (2) is impossible.

The question may arise whether eikonal tomography should be considered to be a geometrical ray theory or a finite frequency theory. The question is motivated by considering globally constrained inverse problems and is somewhat inapt for a locally constrained inversion. We believe, however, that the answer is that eikonal tomography has elements of both. Certainly, the eikonal equation presents information about the local direction of propagation of a wave and is, therefore, not a straight-ray method but is 'geometrical' in character. However, the phase traveltime surfaces that are taken as data in the inversion possess spatially extended sensitivity (finite frequency information), and Lin and Ritzwoller ('On the determination of empirical surface wave sensitivity kernels', manuscript in preparation, 2008) show how approximate empirical finite frequency kernels can be determined from them. Thus, ignoring the second term on the right-hand side of eq. (2) does not equate with rejecting finite frequency information. However, the resulting interpretation of the local gradient of the phase traveltime surface in terms of a wave propagating with a single well-defined direction, $\hat{k}$, is consistent with a single forward scattering approximation. If there were more than one scatterer, that is, multipathing, then the equation could not be interpreted as defining an unambiguous direction of travel at each point. Thus, we do not see Eikonal tomography as a ray method, but summarize it as an approximate finite frequency, geometrical (i.e. bent ray), single forward scattering method.

3 PHASE FRONT TRACKING

Eikonal tomography for ambient noise begins by constructing cross-correlations between each station pair. The ambient noise cross-

correlation method to estimate the Rayleigh and Love wave empirical Green's functions (EGFs) is described by Bensen *et al.* (2007) and Lin *et al.* (2008). We use the method to produce Rayleigh wave EGFs and phase velocity curves between 8 and 40 s period and have processed all available vertical component records from the USArray/TA observed between October 2004 and November 2007. These stations are shown in Fig. 1. The symmetric component cross-correlation (average of positive and negative lag waveforms) between each station pair is used to construct the EGFs.

Each phase traveltime surface is defined relative to a given station location, r_i, which is coincident with the effective source location of the wavefield. If r denotes an arbitrary location, then the traveltime surfaces relative to effective sources i is given by $\tau(r_i, r)$ for $1 \leq i \leq n$, where n is the number of stations. The construction of the phase traveltime surfaces across the array starts by mapping the phase traveltimes in space centred on the effective source locations. Fig. 2(a) presents example great-circle ray paths for an effective source at TA station R06C and Fig. 2(b) shows the EGFs to all other TA stations plotted as a record section band-pass filtered from 15 to 30 s period. The coherence of the information contained in this record section can be seen in wavefield snapshots such as those in Fig. 3, in which the amplitude of the normalized envelope function for each EGF is colour coded. Plots such as these illustrate that the entire Rayleigh wavefield can be seen to propagate away from the effective source. The plot also illustrates how the amplitude of the EGF varies with azimuth, with the largest amplitudes pointing directly towards or away from the coast relative to the central station. Nevertheless, reliable phase times are measurable at nearly all azimuths, which is essential to map the phase traveltime surface.

Phase traveltimes to all stations from an effective source are measured using the method of Lin *et al.* (2008) on each EGF between 8 and 40 s period. For a fixed frequency, the measured phase traveltime is assigned to each station whose EGF has a signal-to-noise ratio (SNR) exceeding 15, where SNR is defined by Bensen
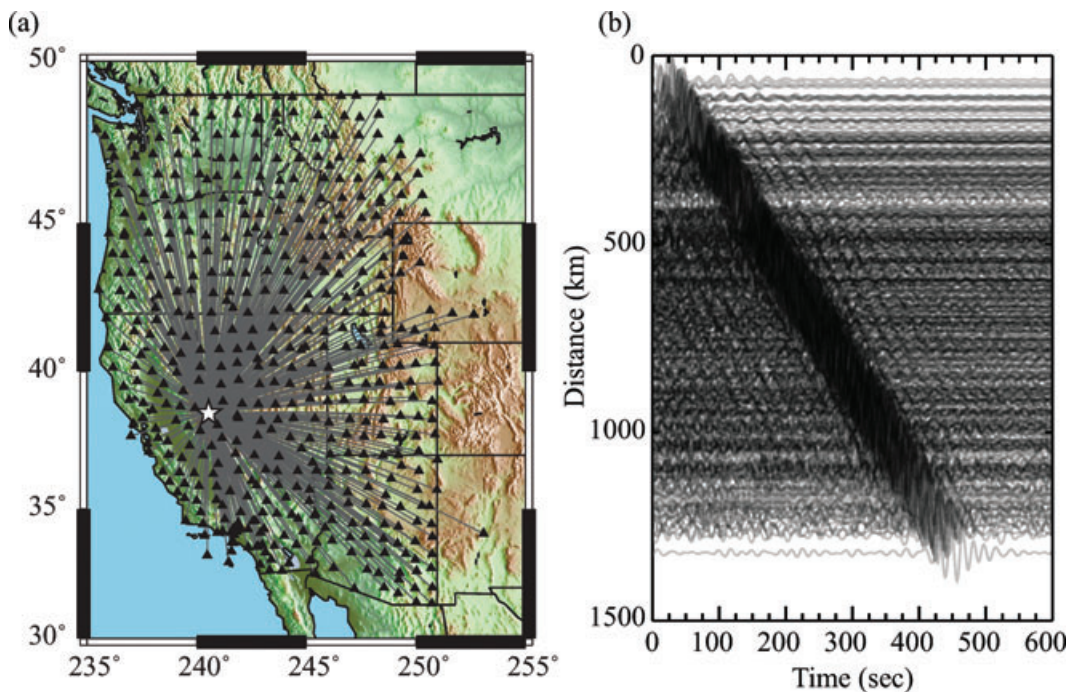
Figure 2. (a) Great circle paths linking station R06C (southeast of Lake Tahoe, identified by the white star) with all TA stations where cross-correlations were obtained. (b) Symmetric component record section for 15–30 s period band-passed vertical–vertical cross-correlations with station R06C in common. More than 450 cross-correlations are shown. Clear move-out near 3 km s^{-1} is observed.
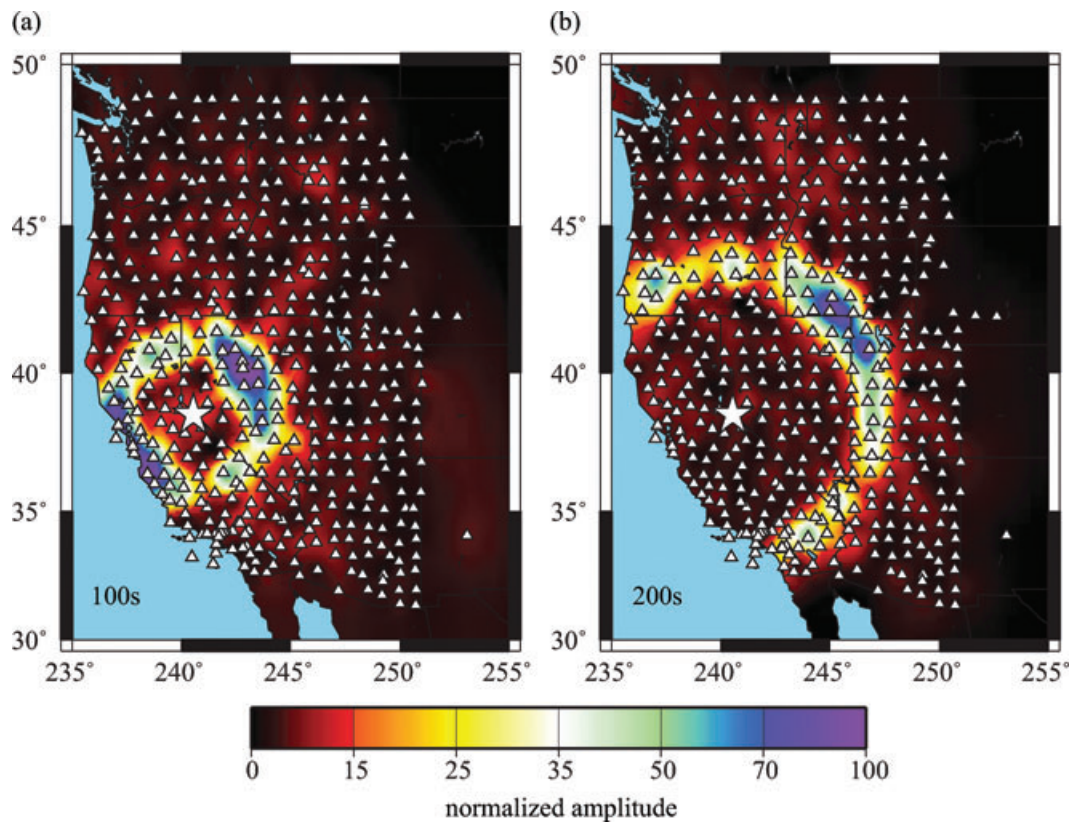
Figure 3. Snapshots of the normalized amplitude of the ambient noise cross-correlation wavefield with TA station R06C (star) in common at the centre. Each of the 15–30 s band-passed cross-correlations is first normalized by the rms of the trailing noise (Lin *et al.* 2008) and fit with an envelope function in the time domain. The resulting normalized envelope functions amplitudes are then interpolated spatially. Two instants in time are shown, illustrating clear move-out and the unequal azimuthal distribution of amplitude.

et al. (2007). To construct a phase traveltime surface, these phase traveltimes must be interpolated onto a finer, regular grid. To do this, we fit a minimum curvature surface onto a 0.2° × 0.2° grid across the western USA. The result for central station R06A for the 24 s Rayleigh wave is shown in Fig. 4(a). Variations in the method of interpolation have minimal effect on the resulting surface, averaging less than 0.2 s except near the central station and on the map's periphery. An example is shown in Fig. 4(b) in which a second interpolation scheme invokes an extra tension term in the surface fitting (Smith & Wessel 1990). The difference near the centre is expected because the real traveltime surface will have singular curvature at the effective source. Accurate modelling of the phase time surface near the source, therefore, would require a different method of interpolation than that used here. In addition, traveltime measurements obtained between stations separated by less than 1–2 wavelengths are less reliable than those from longer paths. Thus, from each traveltime surface we remove the region within two wavelengths of the central station and also any region in which the phase traveltime difference between the two interpolation methods is greater than 1.0 s. Finally, as an added quality control measure, for each location we include measurements from this location only when at least three of the four quadrants of the East–West and North–South axes are occupied by at least one station within 150 km. The resulting truncated phase traveltime map centred on station R06A for the 24 s Rayleigh wave is shown in Fig. 5(a). Several other examples with either a different central station or a different period are also shown in Fig. 5. This method of phase front tracking is not perfect, as several irregularities in the contours of constant traveltime in

Fig. 5(c) testify. Statistical averaging is needed to reduce the effects of these irregularities, as discussed later in Section 4.

The phase front tracking process introduced here is essentially the only place in the eikonal tomography method where the inverter has the freedom to make *ad hoc* choices. The choice of using a minimum curvature surface fitting method as our interpolation scheme minimizes the variation of the gradient and hence gives the smoothest resulting velocity variation. With this interpolation scheme, however, the phase traveltime surface within an area bounded by the three to four closest stations will always have similar gradients. This spatial coherence of the variation of the gradient, as we will discuss later on in Sections 4.2 and 5.1, limits our ability to resolve velocity anomalies much smaller than the station spacing. If higher resolution is desired, a more sophisticated interpolation scheme will be required.

4 EIKONAL TOMOGRAPHY

For the eikonal equation, eq. (3), the magnitude of the gradient of the phase traveltime is simply related to the local phase slowness at position r and the direction of the gradient provides a measure of the direction of propagation of the wave. Taking the gradient on the phase traveltime surface gives the local phase speed as a function of the direction of propagation of the wave. Hence, there is no need for a tomographic inversion. If the eikonal equation is looked at as an inverse problem, the gradient is seen as the inverse operator that maps traveltime observations into model values (phase
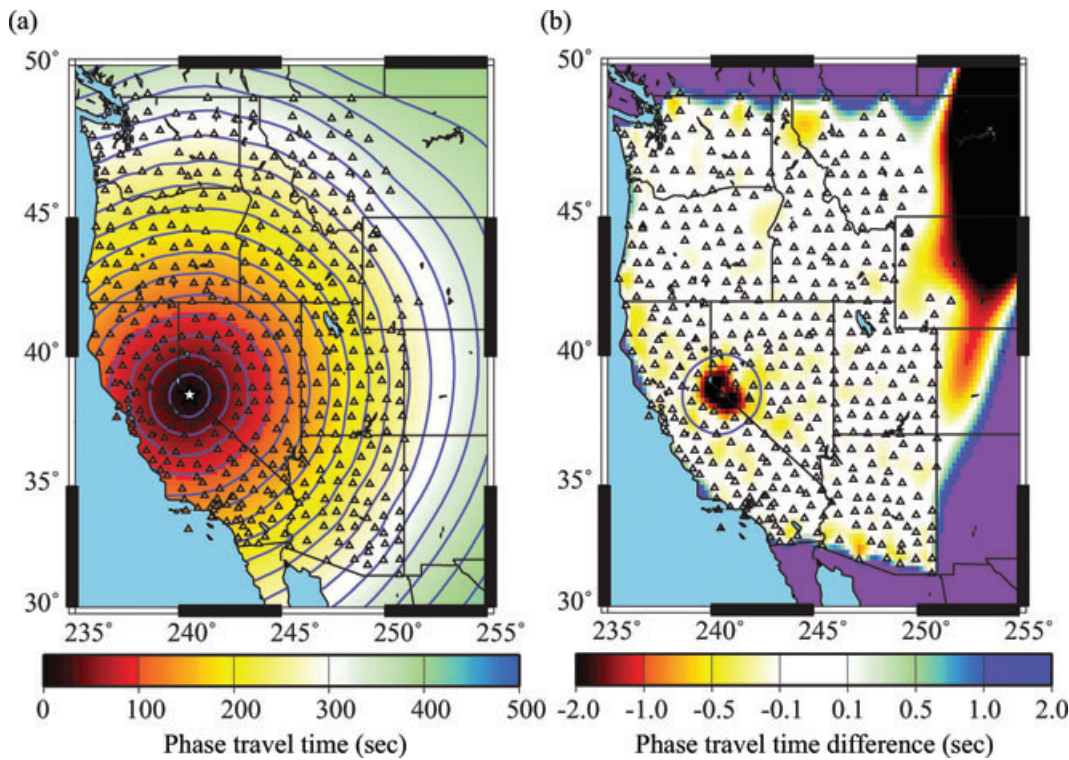
Figure 4. (a) The phase traveltime surface for the 24 s Rayleigh wave centred on TA station R06C (star). Contours are separated by 24 s intervals. (b) The difference in phase speed traveltime using two different phase front interpolation schemes. The 48 s contour is identified with a grey circle centred on station R06C.

slownesses) and is applied without the need first to construct the forward operator.

4.1 Isotropic wave speeds

Fig. 6 shows the result of applying the eikonal equation to the phase traveltime surface for the 24 s Rayleigh wave shown in Fig. 5(a) centred on station R06A. For each individual central station i, the resulting phase speed map is noisy (Fig. 6a) due to imperfections in the phase traveltime map. This is caused by errors in the input phase traveltimes that, in a similar measurement, Lin *et al.* (2008) estimated to be about 1 s, on average. This is a significant error when spacing between stations is small. However, there are n stations, which in the present study for the TA is about 490. This allows the statistics of the phase speed estimates to be determined. For example, Fig. 7(a) shows the 455 Rayleigh wave phase speed measurements at a period of 24 s as a function of the propagation direction for the point in Nevada identified by the star in Fig. 1. To determine the isotropic phase speed and its uncertainty for each point, we first calculate the mean slowness, s_0, and the standard deviation of the mean slowness, σ_{s_0}, from the distribution of slowness measurements, s_i:

$$s_0 = \frac{1}{n} \sum_{i=1}^{n} s_i, \tag{4}$$

$$\sigma_{s_0}^2 = \frac{1}{n(n-1)} \sum_{i=1}^{n} (s_i - s_0)^2, \tag{5}$$

where n is the number of effective sources. This intermediate step properly accounts for error propagation. The isotropic phase speed,

c_0, and its uncertainty, σ_{c_0}, are then determined by

$$c_0 = \frac{1}{s_0} \tag{6}$$

$$\sigma_{c_0} = \frac{1}{s_0^2} \sigma_{s_0}. \tag{7}$$

The local phase speed uncertainty, σ_{c_0}, is mapped for the 24 s Rayleigh wave in Fig. 8(a), where only the region in which the number of measurements is greater than half the total number of the effective sources is shown. The average uncertainty across the map is about 7 m s^{-1} or about 0.2 per cent of the phase speed. Note that this uncertainty estimate only accounts random errors within traveltime measurements. Systematic errors introduced by the tomography method itself will be discussed in Section 5.1.

Example phase speed measurements and the uncertainty map for the 12 s period Rayleigh wave are displayed in Figs 7(b) and 8(b), respectively. Uncertainty at this period is largest along the western and northern edges of the region that is most likely due to small-scale wave front distortion resulting from large velocity contrasts. The average uncertainty is about 8 m s^{-1}, which is slightly larger than that at 24 s. This is not unexpected because the validity of the eikonal equation relies on smoothly varying velocity structures and this is a less robust assumption for surface waves at shorter periods.

The isotropic phase speed maps at periods of 24 s and 12 s are plotted in Figs 9(a) and 10(a), respectively. For comparison, the phase speed maps determined from the phase speed measurements using a traditional tomographic method based on the straight-ray approximation (Barmin *et al.* 2001) are shown in Figs 9(b) and 10(b). Differences between the methods are illustrated in Figs 9(c) and 10(c).
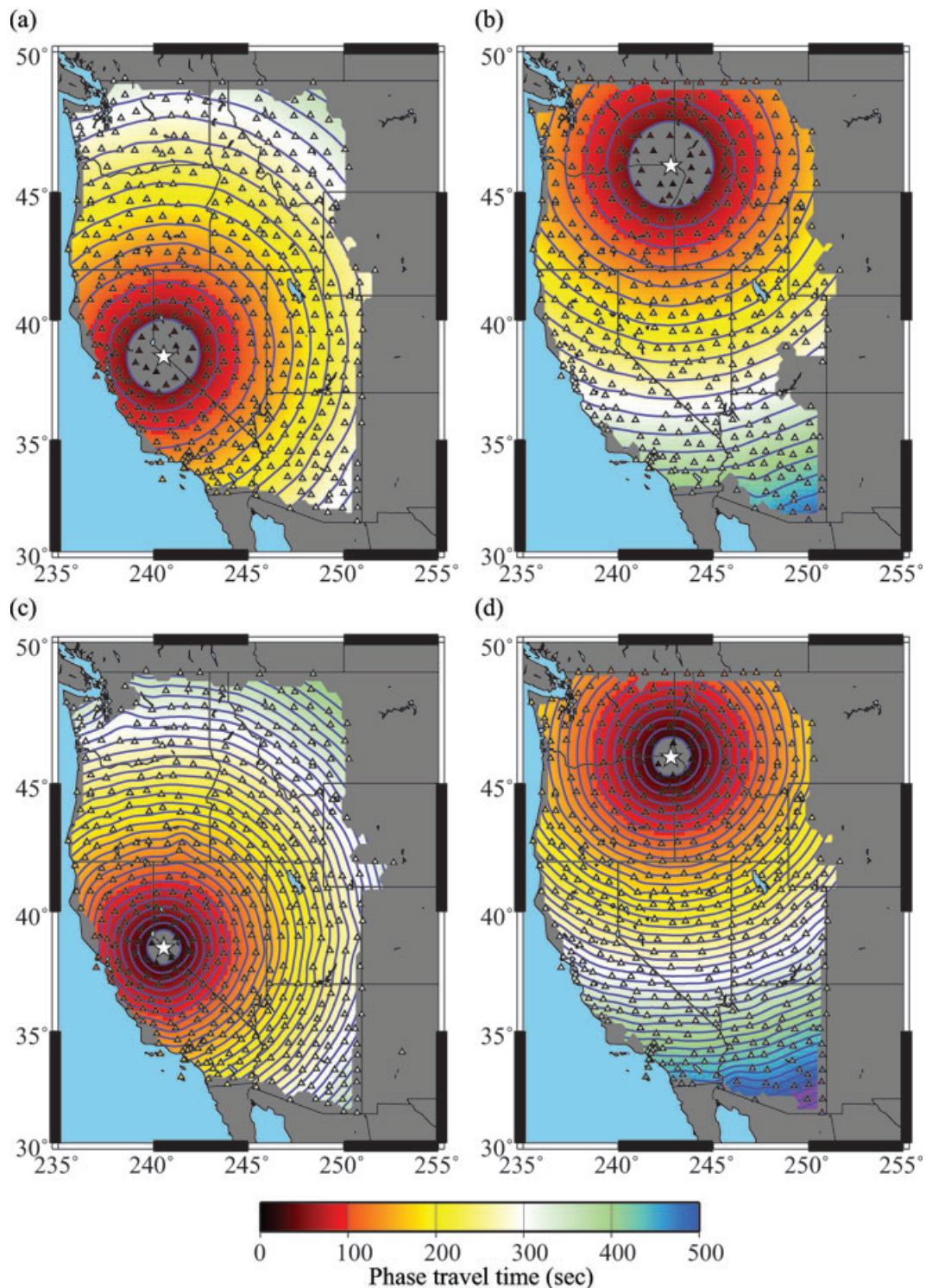
Figure 5. Rayleigh wave phase speed traveltime surfaces at periods of (a, b) 24 s and (c, d) 12 s centred on two 'effective sources': stations R06C (eastern California) and F10A (northeastern Oregon). Traveltime level lines are presented in increments of the wave period. The maps are truncated within two wavelengths of the central station and where the three- out of four-quadrant selection criterion is not satisfied. These two criteria usually take effect only near the periphery of the station coverage.

Agreement between the isotropic maps produced with eikonal tomography and the traditional straight-ray tomography is generally favourable, but there are regions of significant disagreement. At 24 s period, the differences are greatest near the western boundary of the map where eikonal tomography seems to recover crisper, more highly resolved features that correlate better with known geological structures. For the 24 s Rayleigh wave, the phase velocity contrast between the fast and slow anomalies is generally too gentle to make ray paths deviate significantly from great circle paths. This is also indicated in Fig. 6(b) where the average deviation of
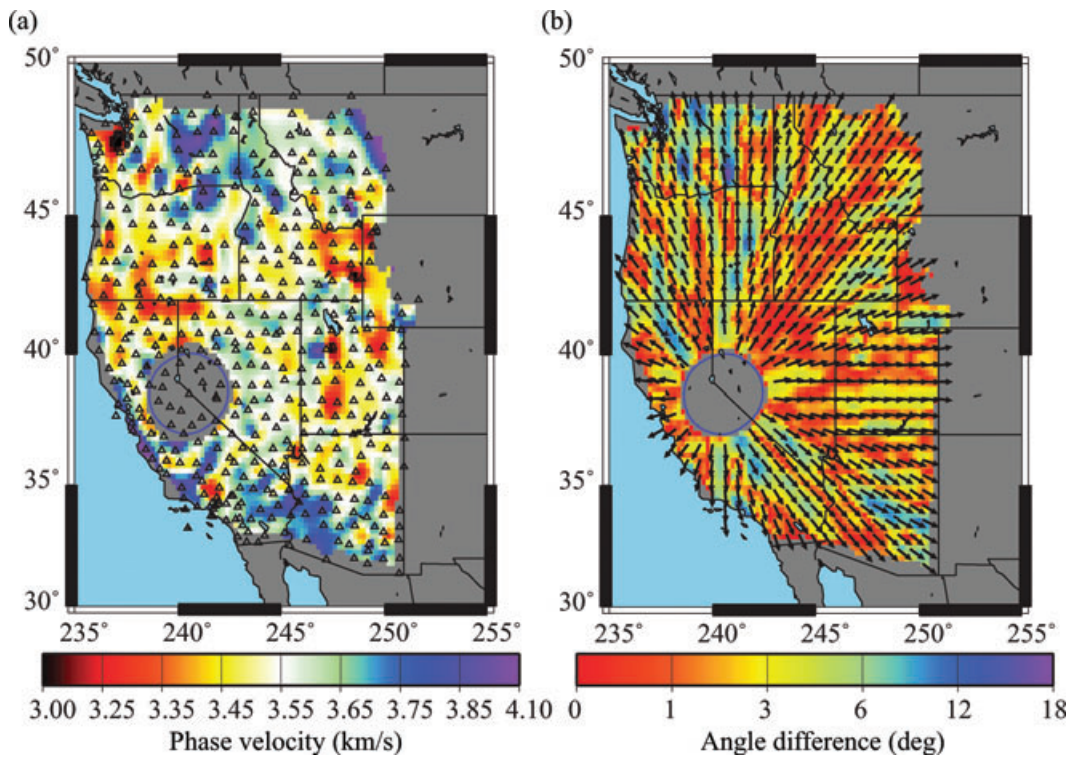
Figure 6. (a) The phase speed inferred from the eikonal equation for the 24 s Rayleigh wave traveltime surface shown in Fig. 5a centred on station R06A. (b) The propagation direction determined from the gradient of the phase traveltime surface at each point is shown with arrows. The difference between the observed propagation direction and the straight-ray prediction (radially away from stations R06A) is shown as the background colour.

propagation direction from the great circle path is only about 3°. It is not likely, therefore, that the differences observed between eikonal and traditional tomography at this period are purely because eikonal tomography accounts for bent rays. Differences more likely result from the regularization applied in the straight-ray inversion, which tends to distort the velocity anomalies near the edges of the map. At 12 s period, however, velocity contrasts are more significant and the off-great-circle effect is more pronounced. The effect of modelling bent rays in eikonal tomography can be seen in at least two features of the 12 s map. First, a lineated anomaly associated with the Cascade Range is better observed with eikonal tomography. Second, eikonal tomography also produces wave speeds that are systematically slower than the straight-ray inversion (Fig. 10c) in most of the region. The bent rays travel faster than the straight rays (Roth *et al.* 1993), and to fit the data equally well with bent rays requires depression of wave speeds, on average. This can be seen clearly in the histograms of differences presented in Fig. 11, where the mean difference between the two 12 s maps is about 10 m s^{-1} (about 0.3 per cent of the phase speed), whereas the 24 s maps differ, on average, only by $\sim$5 m s^{-1}.

4.2 Coherence length of the measurements

Traditional estimates of resolution typically are based on applying the inverse operator (relating observations to model variables) to the forward operator (relating model variables to observations) in an inverse problem. With eikonal tomography, neither an inverse nor a forward operator is constructed explicitly, so resolution is not straightforward to determine. Checkerboard tests are possible, but numerical simulations would need to accurately calculate the phase traveltime between each station pair.

We take a different approach and attempt to estimate the resolution based on the coherence length of the measurements. To do so, we first estimate the statistical correlation, ρ, of slowness measurements between locations j and k by

$$\rho_{jk} = \frac{\left(\sum_{i=1}^{n} (s_{ji} - s_{j0})(s_{ki} - s_{k0}) \right)^2}{\sum_{i=1}^{n} (s_{ji} - s_{j0})^2 \sum_{i=1}^{n} (s_{ki} - s_{k0})^2}, \tag{8}$$

where i is the index of the effective sources and s_{j0} and s_{k0} are the mean slowness at locations j and k, respectively. The statistical correlation, ρ, varies between 0 and 1 and represents the degree of coherence or independence between the measurements made at the two locations. Using the point in central Nevada (Fig. 1) as an example again, the statistical correlation between the phase speed observations at that point and the neighbouring points is summarized as a correlation surface shown in Fig. 12(a). We follow Barmin *et al.* (2001) and estimate the coherence length of the measurements by fitting the correlation surface with a cone, where the base radius of the cone is taken as the coherence length estimate R.

Although this is different from the traditional definition of resolution, it does provide information about the length scale of features that can be resolved in a region. The coherence length estimated in this way for the 24 s Rayleigh wave is shown in Fig. 12(b). In most regions, coherence length is somewhat smaller than the average inter-station spacing of 70 km across the western USA. Although this result is comparable to the resolution estimated by the straight-ray tomography (Lin *et al.* 2008), there are fundamental differences between the two. When the observed phase traveltimes are affected by a velocity structure much smaller than the inter-station distance, without a more sophisticated interpolation scheme, the minimum

(a)

(b)
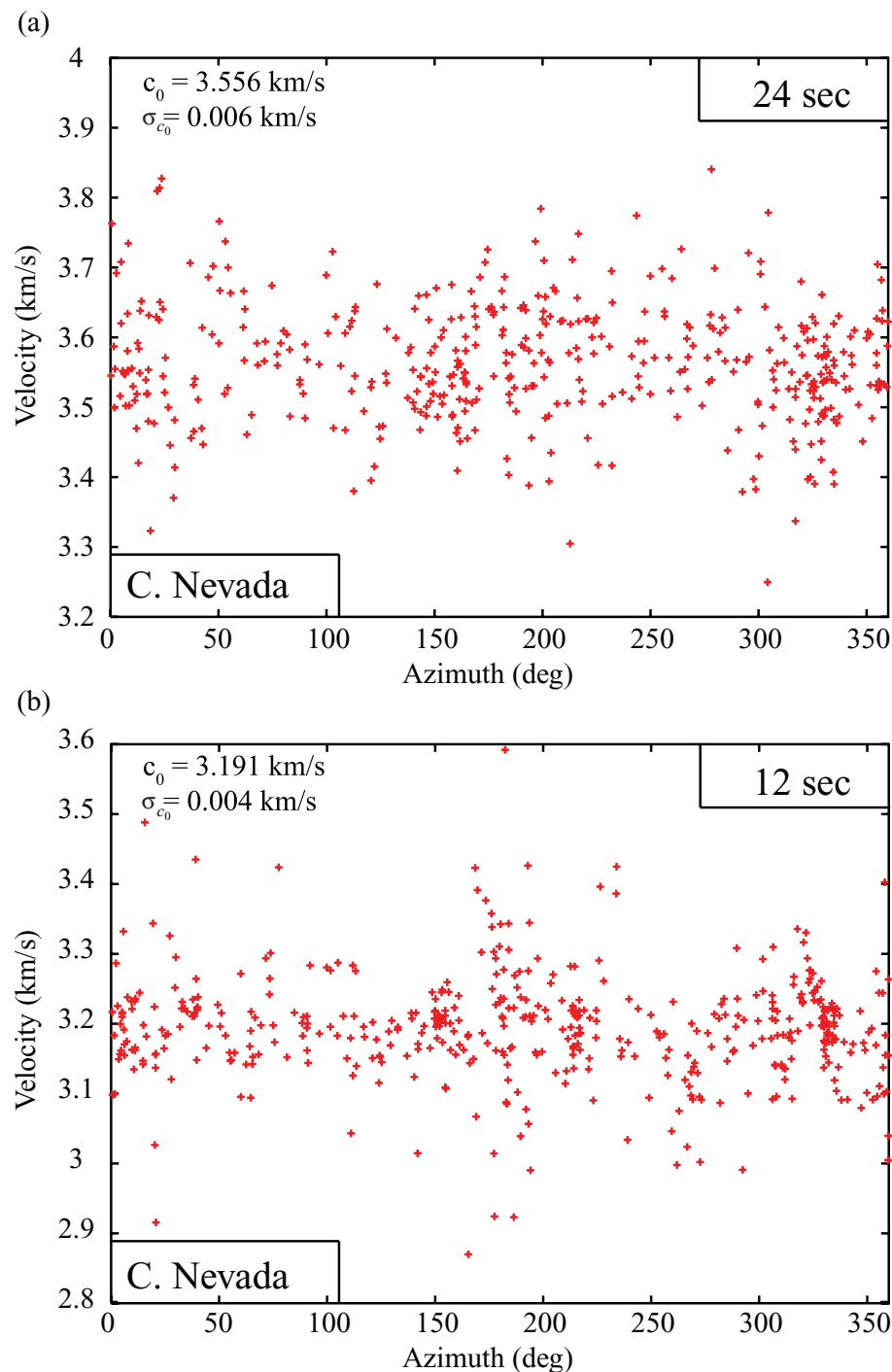
Figure 7. (a) Example of the azimuthal distribution of the Rayleigh wave phase velocity measurements at 24 s period for the point in central Nevada indicated by the star in Fig. 1. (b) Same as (a), but for the 12 s Rayleigh wave phase speed at the same location. The mean and standard deviation of the mean are identified at upper left in each panel.

curvature fitting method we use will smear the traveltime anomalies to an area confined by the few closest nearby stations. This smearing effect is further evidenced in our synthetic tests in Section 5.1. Thus, the station spacing constrains the coherence length as well as the smallest scale of structure that can be confidently resolved. Increasing the number of effective sources will tend to reduce the estimated uncertainty, but most likely will have a little impact on the coherence length.

4.3 Azimuthal anisotropy

Eikonal tomography also provides an estimate of azimuthal anisotropy. In traditional surface wave inversions, it is commonly assumed that the Rayleigh wave phase speed exhibits the following functional dependence on azimuth, which is derived based on theoretical studies of weakly anisotropic media (Smith & Dahlen 1973):
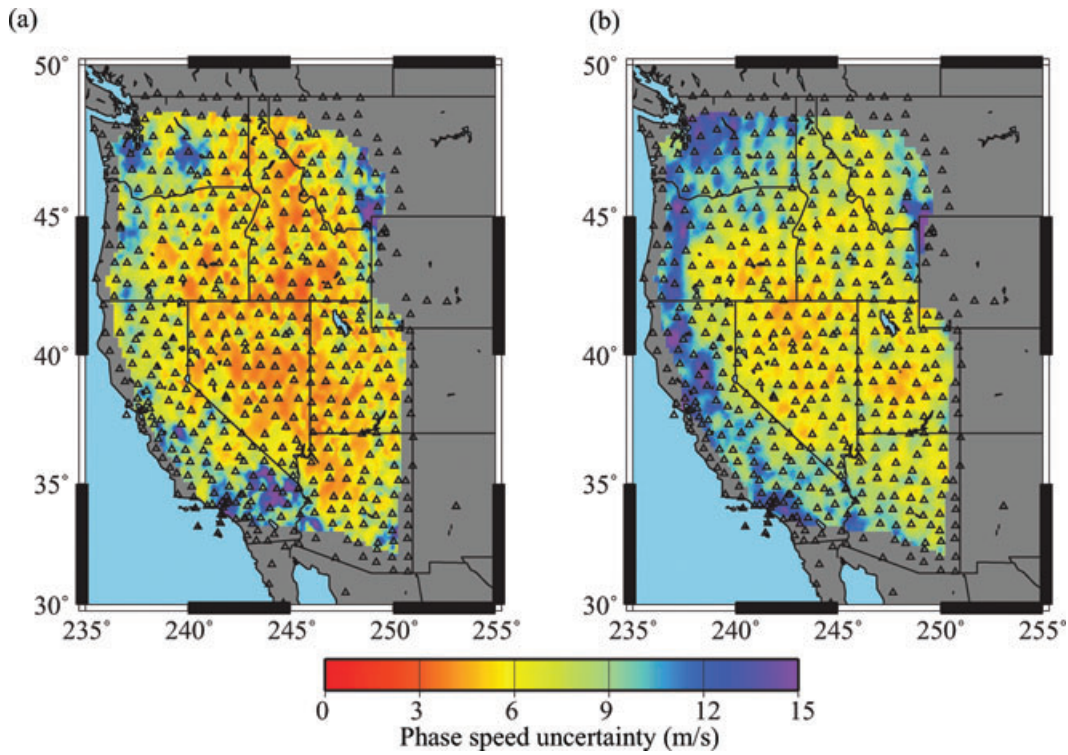
Figure 8. (a) The 24 s period isotropic Rayleigh wave phase speed uncertainty map, determined from the distribution of phase speed measurements based on applying the eikonal equation to each of the phase traveltime maps at each point. (b) The 12 s isotropic Rayleigh wave phase speed uncertainty map.
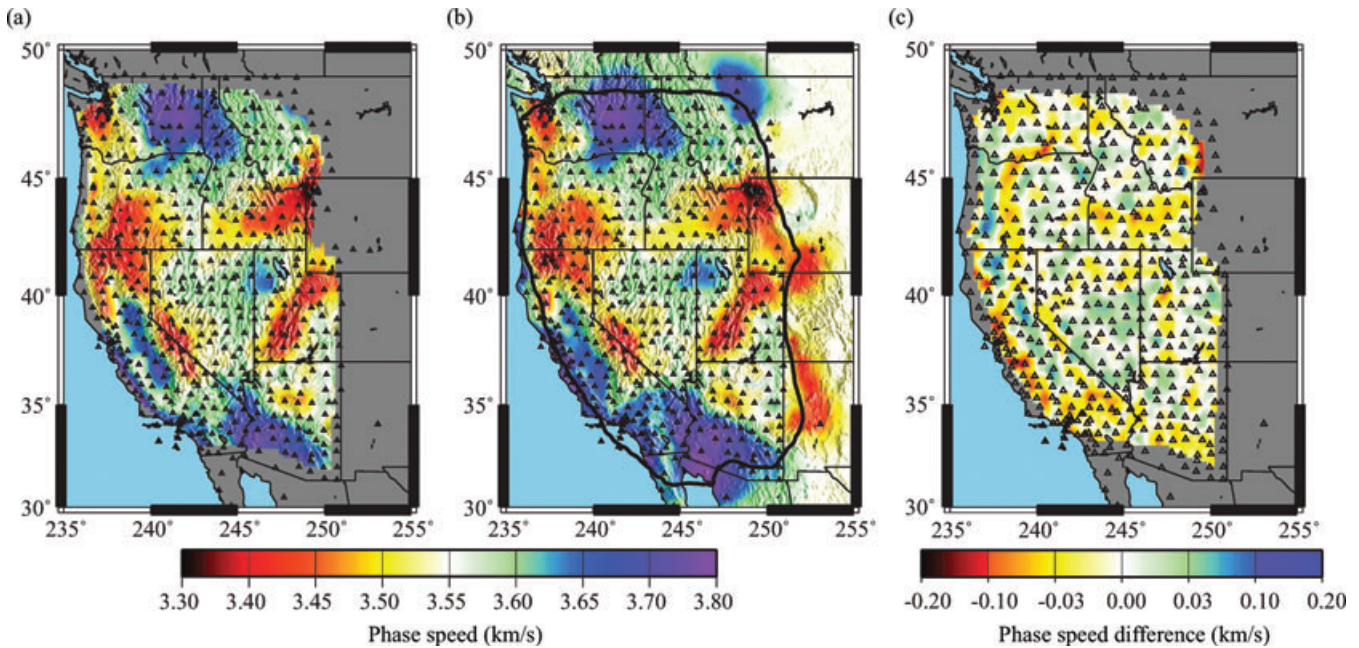

Figure 9. (a) The 24 s Rayleigh wave isotropic phase speed map derived from eikonal tomography. The isotropic phase speed at each point is calculated from the distribution of local phase speeds determined from each of the phase traveltime maps. (b) Same as (a), but the straight-ray inversion of Barmin *et al.* (2001) is used. The black line is the 100 km resolution contour. (c) The difference between eikonal and straight-ray tomography is shown where positive values indicate that the eikonal tomography gives a higher local phase speed.

$$c(\psi) = c_0 + A\cos[2(\psi - \varphi)] + B\cos[4(\psi - \alpha)], \qquad (9)$$

where ψ is the azimuthal angle measured positive clockwise from north, A and B are the amplitude of anisotropy and φ and α define the orientation of the anisotropic fast axes for the 2ψ and 4ψ compo-

nents of anisotropy. Although the estimated 2ψ fast directions may be robust in the traditional inversion, the amplitude of the anisotropy almost inevitably depends on the regularization parameters chosen (e.g. Smith *et al.* 2004). In eikonal tomography, the velocity as a function of azimuth of the wave is measured directly and it is
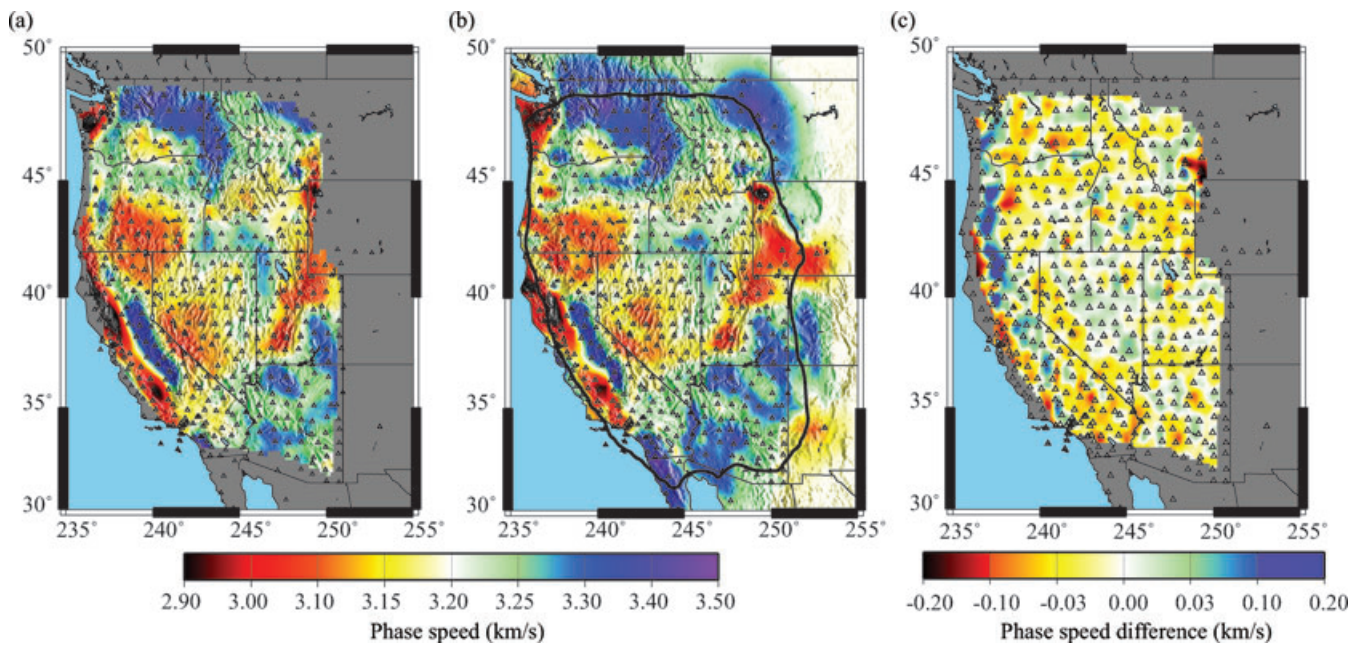
Figure 10. The same as Fig. 9, but for the 12 s Rayleigh wave. The result of eikonal tomography is slightly slower (yellow-red shades), on average, than the straight-ray tomography because it models off-great-circle propagation.
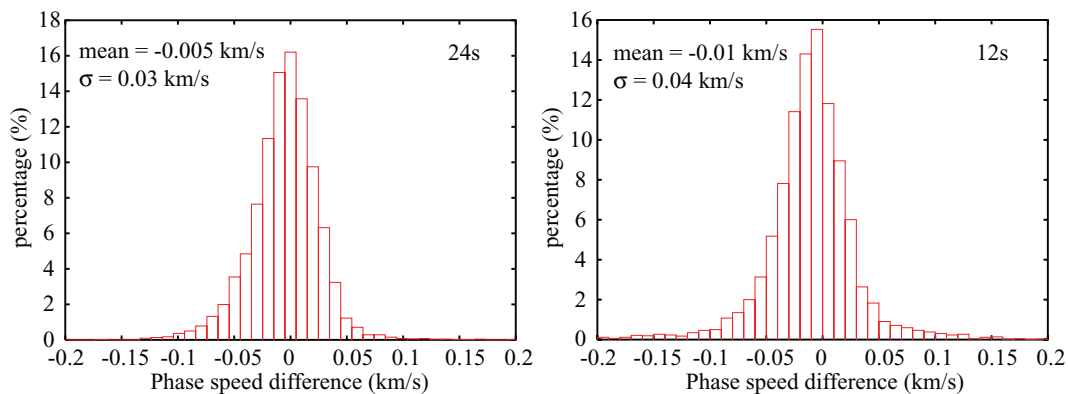

Figure 11. Normalized histograms of the Rayleigh wave phase speed difference across the studied region between eikonal tomography and straight-ray tomography at 12 and 24 s period, respectively. The mean differences result because eikonal tomography models off-great-circle propagation, which is more significant at 12 s than 24 s period.

then determined if the relationship reflects a simple function of azimuth.

As with the measurement of isotropic phase velocity, the estimation of anisotropy begins with the set of phase speeds estimated at a single spatial location from the set of phase speed traveltime maps segregated by azimuth, as in the example shown in Fig. 7(a) for the 24 s Rayleigh wave for a point in central Nevada. Due to phase traveltime errors in the maps, the measured phase speeds are significantly scattered and any azimuthally dependent trend is obscured. Scatter is reduced substantially by stacking and binning in two stages. First, we combine the azimuthally dependent phase speed measurements obtained at the target point with measurements at the eight surrounding spatial points (3×3 grid with the target point at the centre). We use a 0.6° grid separation approximately equal to the coherence length estimate described in the last section, which effectively guarantees that measurements are statistically independent from one another. To reduce mapping the lateral variation of

isotropic phase speed into azimuthal anisotropy, we remove the isotropic speed difference between each point and the centre point of the 3×3 grid for all of the measurements. This stacking process increases the number of measurements for the centre point, but does so at the expense of reducing spatial resolution. Second, we combine all of the azimuthally dependent phase speed measurements in each 20° azimuthal bin into a mean speed and its standard deviation of the mean for that bin. Here, again, the mean slowness and the standard deviation of the mean slowness are first calculated and then converted to the mean speed and its uncertainty.

Fig. 13 shows examples for four different geographical locations of the stacked azimuthally dependent phase speed measurements with their uncertainties for the 24 s Rayleigh wave. For the examples in Utah and Nevada, Figs 13(a) and (b), where good azimuthal data coverage exists, a clear 2ψ variation is observed for the entire 360° of azimuth. On the other hand, Figs 13(c) and (d) show two examples near the western boundary of the map where azimuthal coverage
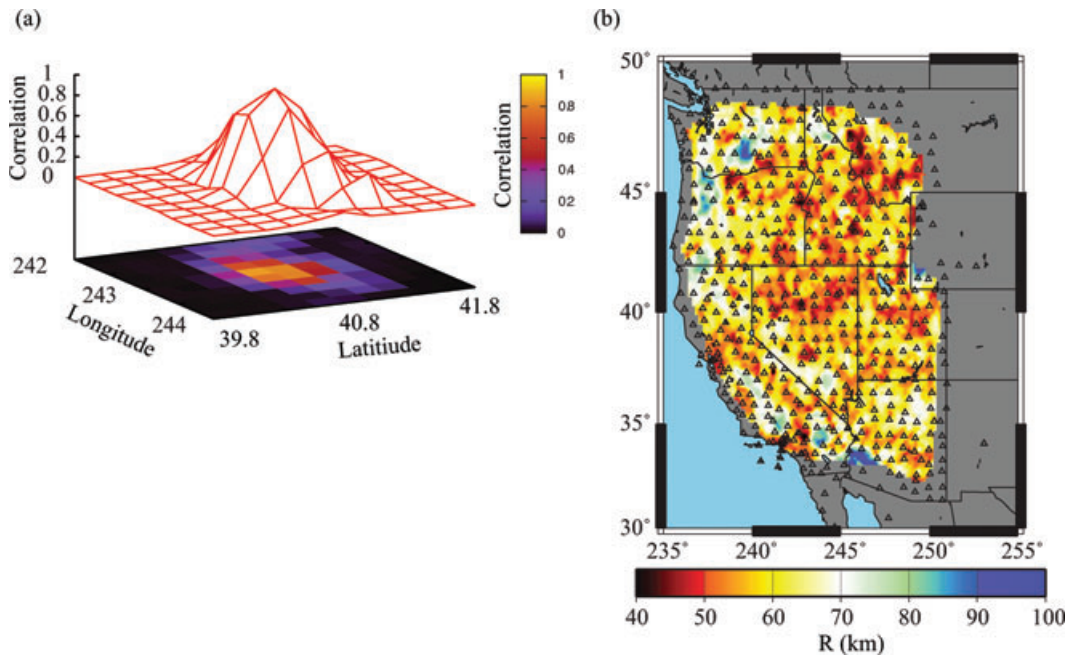
Figure 12. (a) An example of the spatial coherence of the measurements for the 24 s Rayleigh wave at the point in central Nevada indicated by the star in Fig. 1. (b) The radius (R) of the cone fit to the coherence surface at each location, which bears a similarity to resolution.
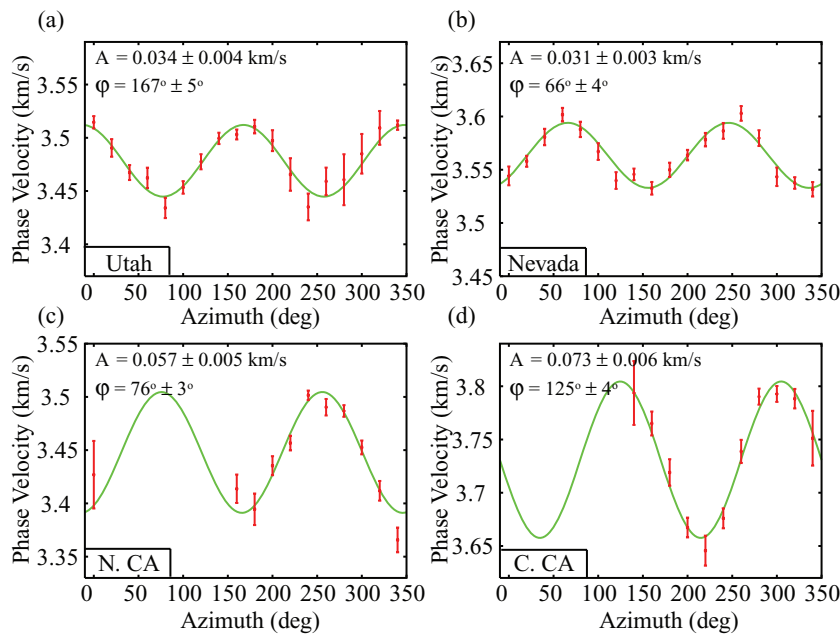

Figure 13. Examples of the azimuthal dependence of phase velocity measurements for the 24 s Rayleigh wave at four points in the western USA where large amplitude 2ψ azimuthal variation can be observed: (a) Utah, (b) Nevada, (c) northern California and (d) central California. The locations are indicated by the circle, star, square, and diamond in Fig. 1, respectively. Error bars are estimated based on the distribution of phase velocity measurements in each $20°$ azimuthal bin for the given location and its eight nearest neighbouring grid points. For each case, the solid line is the best fit of the 2ψ azimuthal variation.

is limited. Nevertheless, the 2ψ velocity signal is still observed robustly because measurements cover at least $180°$. Based on these observations, for each period and location, we adopt the assumption of a weakly anisotropic medium, fit the results with the 2ψ part of the cosinusoid and use it to estimate the amplitude and fast direction of anisotropy with associated uncertainties. Here, robust statistics are used. Measurements that cannot be fit within 2 standard deviations

are removed to minimize the effect of significant outliers, but the difference between the robust statistics and non-robust statistics is small overall. Adding the 4ψ term does not improve the data fit appreciably, which indicates that the 4ψ variation of Rayleigh waves is weaker and our data set is not sufficient to constrain it. The observed 2ψ azimuthal anisotropy exhibits different amplitudes and fast directions in different locations. This minimizes concern about
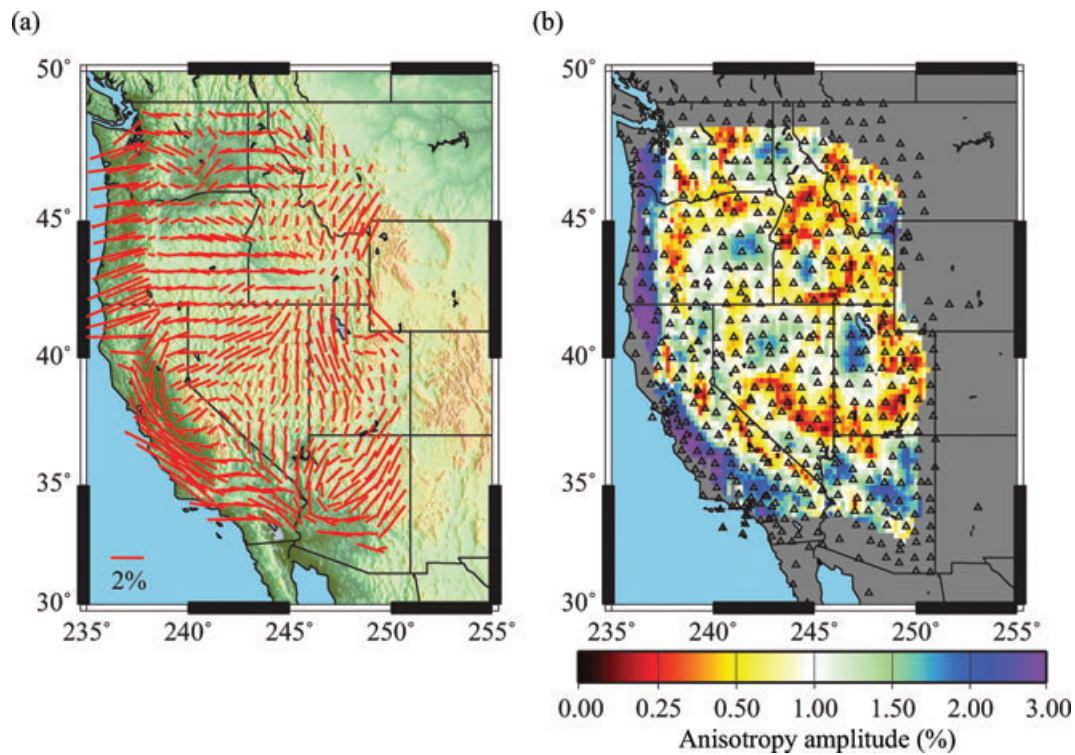
Figure 14. (a) The 24 s period Rayleigh wave azimuthal anisotropy fast axis directions and peak-to-peak amplitudes, $2A/c_0$, which are proportional to the length of the bars. (b) Peak-to-peak amplitude of anisotropy presented in per cent.
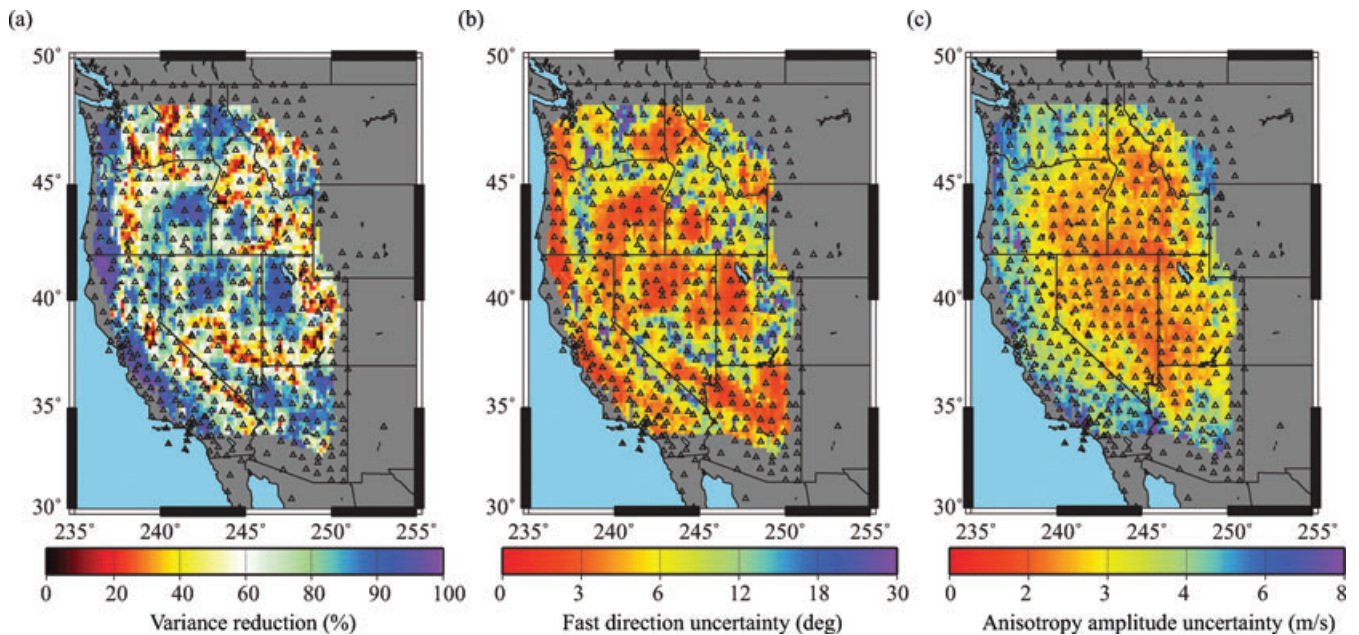

Figure 15. (a) Variance reduction of the 24 s Rayleigh wave 2ψ azimuthal anisotropy relative to the isotropic speed at each point. (b) The uncertainty in the angle of the fast direction, φ. (c) The uncertainty of the amplitude of anisotropy.

systematic errors in the input phase traveltimes due to azimuthally inhomogeneous ambient noise sources that could result in a uniform fast direction for the entire region.

Azimuthal anisotropy for the 24 s Rayleigh wave is summarized in Fig. 14a. The peak-to-peak amplitude of anisotropy is presented in Fig. 14(b). Fig. 15(a) presents the variance reduction after introducing the 2ψ anisotropy term. Significant improvements

(>80 per cent) are observed over extended regions, which not only indicates the robustness of the measurements but also suggests that azimuthal anisotropy is a general feature of Rayleigh waves in the western USA. We note that the regions with poor variance reduction (<40 per cent) are generally accompanied by weak anisotropy (<0.5 per cent), which may be a real feature or may be due to a spatially rapid and unresolvable change in fast direction. The estimated
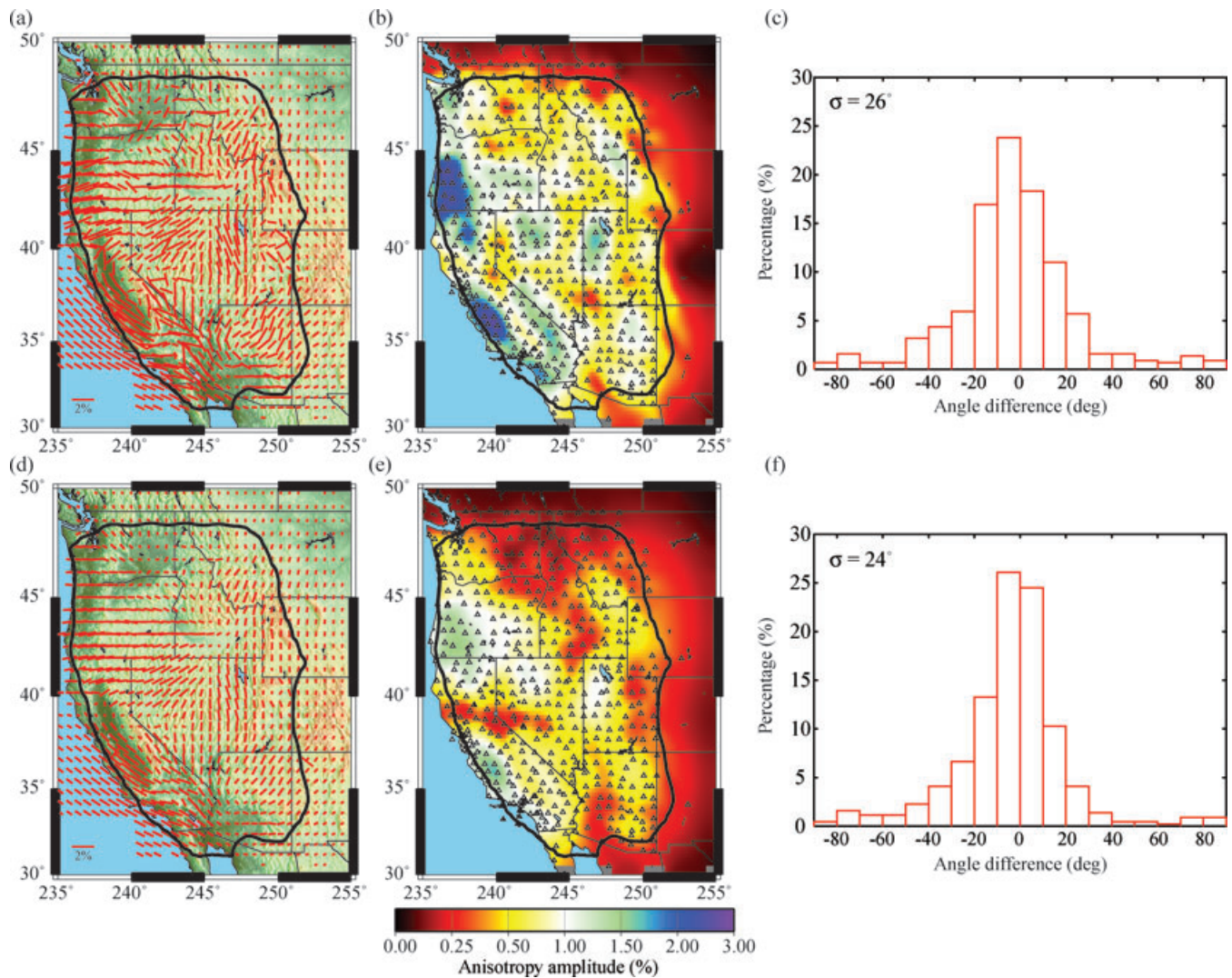
Figure 16. (a)–(b) Same as Figs 14(a) and (b), but here the 24 s Rayleigh wave azimuthal anisotropy result is determined with the traditional straight-ray method of Barmin *et al.* (2001) with a regularization chosen to approximate the amplitudes in Fig. 14b. The black line is the 100 km resolution contour. (c) The normalized histogram of the difference in fast directions between the eikonal tomography result (Fig. 14a) and the straight-ray tomography result. (d)–(f) Same as (a)–(c) but with stronger smoothing regularization. Patterns of anisotropy remain largely unchanged, but amplitudes diminish with greater the damping.

uncertainty of the observed azimuthal anisotropy fast directions and amplitudes are summarized in Figs 15(b) and (c), respectively. As in traditional anisotropy tomography, the fast directions are generally robust features. We estimate the uncertainties of the fast directions to be less than 6° in most of regions. Again, regions with larger uncertainties in the fast direction generally result from weak anisotropy. Uncertainties in the amplitude of anisotropy are generally smaller (<3 m s^{-1} or 0.1 per cent of the isotropic phase speed) in regions with nearly complete azimuthal data coverage than near the periphery of the studied region where only part of entire azimuthal range has measurements.

For comparison, the 2ψ 24 s Rayleigh wave phase speed anisotropy determined by traditional straight-ray inversion (e.g. Barmin *et al.* 2001) with two different smoothing strengths is summarized in Figs 16(a) and (d) and with amplitudes plotted in Figs 16(b) and (e). The difference in fast directions compared to eikonal tomography is also summarized as histograms in Figs 16(c) and (f), where only regions with anisotropy amplitude larger than 0.5 per cent in the eikonal tomography are included. Overall, the ob-

served anisotropy fast direction patterns are consistent between the two traditional inversions and the eikonal tomography inversion. This is not unexpected because the off-great-circle effect is relatively weak at 24 s period. The anisotropy amplitude is significantly smaller in the second case of the straight-ray inversion, which indicates that the smoothing regularization was too strong. Most places with a significant difference in fast directions ($>30°$) occur near a transition in the fast direction of anisotropy where the results of neither model are robust.

With the traditional inversion method, it is tricky to select the right regularization parameters, and methods to do so are typically *ad hoc*. Many studies use trade-off curves between misfit and model roughness or the number of degrees of freedom to select the preferred regularization parameters (e.g. Boschi 2006; Zhou *et al.* 2005). This is, however, difficult for azimuthal anisotropy because by including 2ψ azimuthal anisotropy, for example, the number of degrees of freedom at each node increases to 3 from 1 for an isotropic wave speed inversion despite the fact that the improvement in misfit is usually modest. For traditional tomography
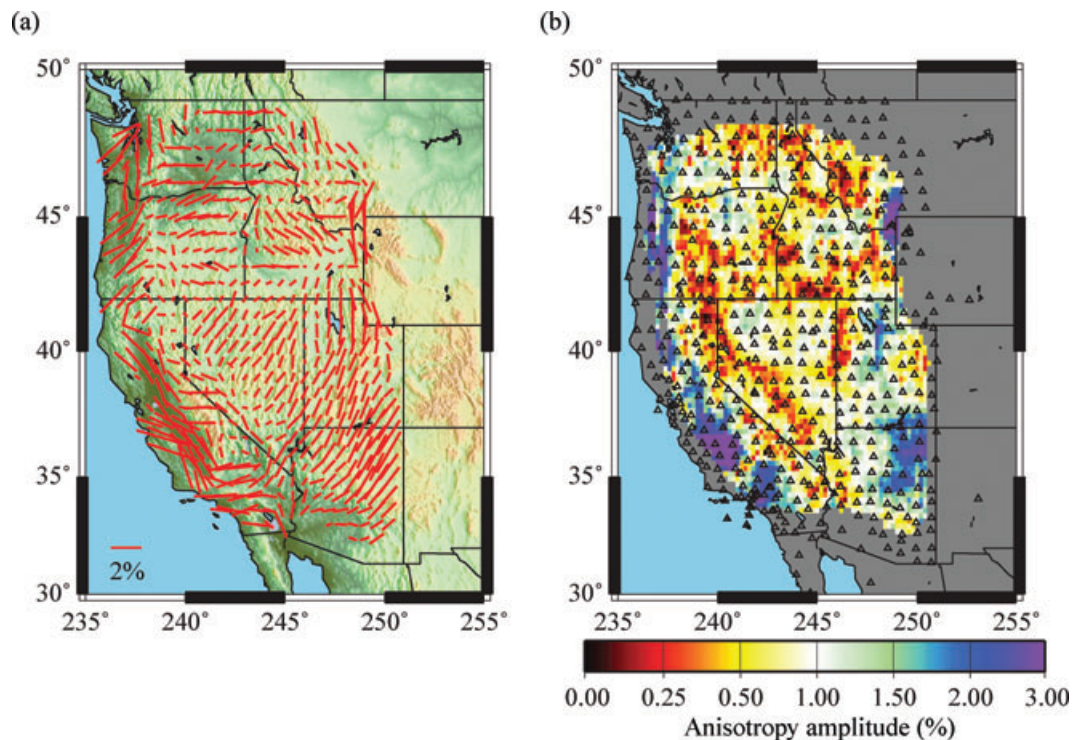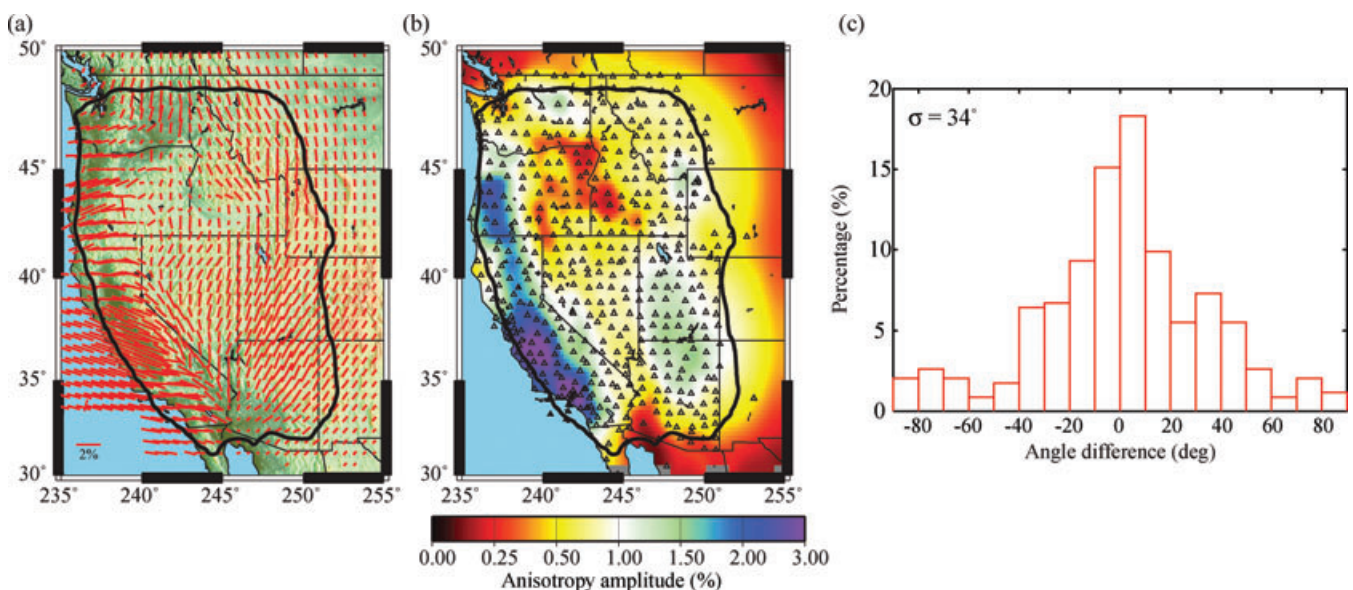
Figure 17. Same as Fig. 14, but for the 12 s Rayleigh wave.

applied to the 24 s Rayleigh wave phase speed data, the standard deviation of traveltime misfit drops from around 3 s for a homogeneous reference model to 1.57 s after the straight-ray isotropic speed inversion (Fig. 9b). However, it then only decreases slightly to 1.53 s and 1.54 s for the two 2ψ azimuthal anisotropy inversions (Figs 16a and d). With eikonal tomography, through the stacking and binning process, we effectively separate the velocity variation due to measurement error from anisotropy and are able to inspect the observed azimuthally dependent phase speed measurements visually. In this way, the observed variance reduction is statistically meaningful and can be used to indicate the confidence level of the result.

The 12 s Rayleigh wave 2ψ azimuthal anisotropy results based on eikonal tomography are presented in Fig. 17. Overall, the anisotropy is robustly measured despite the fact that the amplitudes of anisotropy are generally weaker and the fast direction pattern is slightly different than the 24 s results. Fig. 18(a) shows an example of the 12 s 2ψ azimuthal anisotropy determined by our traditional straight-ray inversion with anisotropy amplitude plotted in Fig. 18(b). The difference in fast directions compared to the

Figure 18. Same as Fig. 16, but for the 12 s Rayleigh wave. Agreement between the eikonal and straight-ray tomography is worse at 12 s than 24 s because of the larger effect of off-great-circle propagation.

eikonal tomography is summarized in the histogram in Fig. 18(c). Compared with 24 s period, more significant differences in both the fast directions and the amplitude patterns are observed, particularly near regions where there are discrepancies between the two isotropic wave speed maps (Fig. 10). We believe that the off-great-circle effect, which is more important for 12 s Rayleigh waves, is responsible for most of the observed differences between the methods at this period.

5 DISCUSSION

5.1 Numerical simulations to test for systematic errors

To assess possible systematic errors due to approximations in the eikonal tomography method, which include both dropping the amplitude term in eq. (2) and using a minimum curvature surface fitting method to interpolate the phase traveltime surface, we perform a series of 2-D finite difference simulations to solve the Helmholtz equation numerically and obtain a synthetic traveltime database. We invert this database based on eikonal tomography and evaluate the difference between the tomography result and the input phase speed model to constrain the systematic errors.

Two cases, 12 and 36 s periods, are studied here that represent periods at the short- and long-period ends of our study. The isotropic wave speed maps derived from the USArray data set and eikonal tomography are used here as the input models (Figs 19a and 20a). In each simulation, a periodic source centred at one station location is used to generate a single frequency out-going wave that propagates in the 2-D medium of the input wave speed model. The resulting waveforms observed at all other station locations are used to measure the phase traveltimes between those stations and the effective source, where the measurements are made when the waveform stabilizes after several cycles. Although synthetic traveltimes are available between all station pairs, to be comparable with the inversion with real data, only those measurements included in the original data sets are included. We follow the same procedure described in Sections 3 and 4 to invert these synthetic data sets based on eikonal tomography and both the isotropic and anisotropy results are shown in Figs 19(b), (c) and 20(b), (c).

Unsurprisingly, the resulting isotropic speed maps, for both 12 and 36 s, closely replicate the large scale features of the input models, although small-scale anomalies in the input models tend to be smoothed out. This smoothing effect is expected, as discussed in Section 4.2. To assess other systematic errors, we smooth the input models with a spatial Gaussian filters with a standard deviation of 35 km and summarize the differences between the isotropic inversion results and the smoothed input models in Figs 19(d) and 20(d). Deviations are most significant near the periphery of our station coverage, particularly near regions with large velocity contrasts such as regions near the Central Valley of California and the Sierra Nevada for the 12 s case and the Southern Sierra Nevada for the 36 s case where delamination is inferred by previous studies (e.g. Yang & Forsyth 2006). Similar anisotropic deviations are also observed for both the 12 and 36 s cases (Figs 19c and 20c), where the amplitude of the anisotropy tends to correlate with the observed isotropic wave speed deviations. This suggests that rapid velocity contrasts near the periphery of the maps tend to distort the wave front dramatically and the method becomes less robust. The observed isotropic (Figs 19d and 20d) and anisotropic (Figs 19c and 20c) deviations are also summarized as histograms in Figs 19(e), 20(e), 19(f) and 20(f), respectively.

We test whether we can reduce these deviations by including amplitude measurements in our synthetic data sets. Again, minimum curvature surface fitting is used to first interpolate the synthetic amplitudes measured at each station to construct amplitude surfaces before calculating the second term in eq. (2). The effect of including the amplitude term is in general unnoticeable, which is partly because the surface interpolation schemes we use here provides relatively smooth amplitude surfaces that tend to minimize the Laplacian term in eq. (2). This is inevitable unless a denser station network is available.

The observed isotropic and anisotropic amplitude deviations, with standard deviations, approximately equal to 10 m s^{-1} and 0.3 per cent peak-to-peak (or 6 m s^{-1} assuming 4 km s^{-1} isotropic speed; Figs 19e and f and 20e, and f), respectively, are generally small relative to the observed isotropic velocity variations (Figs 9a and 10a) and anisotropy amplitudes (Figs 14b and 17b). They are, however, approximately on the same scale as the estimated uncertainties derived from our statistical analysis (Figs 8a, b and 15c). This suggests that the estimated uncertainties described in Section 4, which only accounts the random measurement errors, may underestimate the difference between the tomography results and the real medium properties. When numerical solutions are available, such as here, systematic errors due to the tomography method can be numerically estimated and a better estimation of the uncertainty can be made by summing the effects of the systematic and random measurement errors. However, this may prove impractical due to the heavy computation required. Considering the positive correlation between random (Figs 8a, b and 15c) and systematic errors (Figs 19c, d and 20c, d), here we propose 1.5 as a rule of thumb scaling factor to multiply the random error uncertainty estimations to provide a more realistic uncertainty estimate.

We would like to emphasis here that the systematic errors discussed here are solely due to the imperfection in the tomography method and do not account for systematic errors in traveltime measurements. Systematic traveltime measurement errors can arise, for example, due to timing errors or inhomogeneous noise source distributions for noise cross-correlation measurements. We believe that the effect of inhomogeneous noise source distribution in our results is small, however. Traveltime errors due to inhomogeneous source distribution are likely similar between nearby stations. When the gradient is calculated in eikonal tomography, these errors will cancel.

5.2 Advantages and limitations of eikonal tomography

There are several significant advantages of eikonal tomography over traditional surface wave tomography methods.

First, the implementation of the inverse operator for eikonal tomography depends on operations to the data without explicitly solving the forward problem. For a wave propagating in an inhomogeneous medium, the observed wave properties such as phase traveltime are only linearly related to the local velocity structure when structural perturbations are small. In other words, any linearized forward operator, such as the ray or finite frequency sensitivity integrals, and the inverse operator derived from it can only be considered approximate. Errors caused by this linearization are often overlooked or are unknown, and moving beyond them requires iterative simulations that are computationally expensive. Eikonal tomography extracts the information about local velocity structure directly from the data without explicitly constructing the forward operator. It, therefore, finesses the non-linear nature of the problem
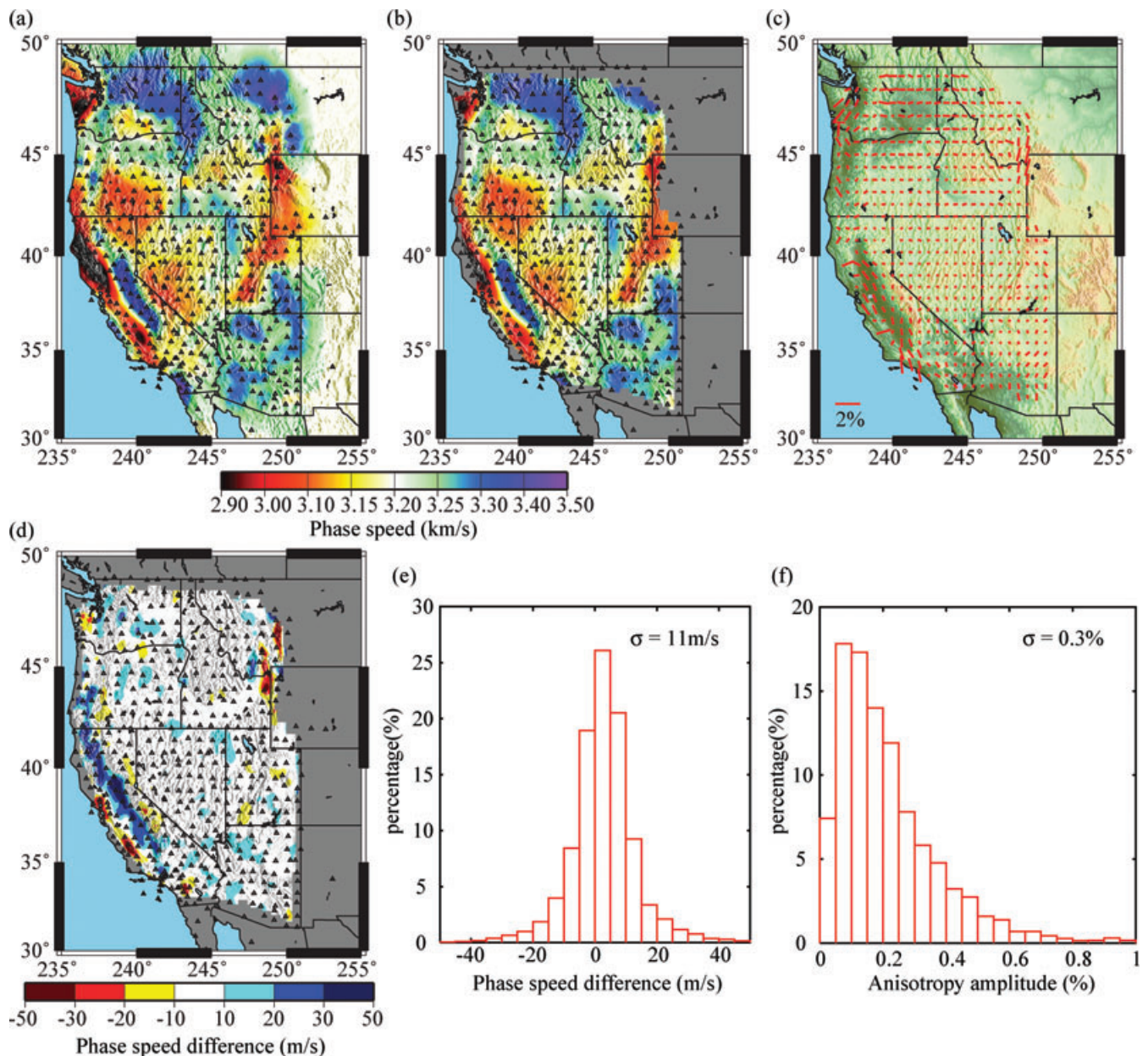
Figure 19. (a) The input wave speed model for the 12 s simulations. The model is derived based on the isotropic result of eikonal tomography with real data (Fig. 10a) where the model gradually smears into a homogeneous model near the boundary of the station coverage. (b) and (c) The isotropic and anisotropic inversion results from eikonal tomography with the 12 s synthetic data set. (d) The difference between the synthetic inversion and smoothed input model where positive values indicate that the synthetic inversion gives a higher local phase speed. (e) Normalized histogram of the speed difference across the studied region between the synthetic inversion and the smoothed input model. (f) Normalized histogram of the anisotropic peak-to-peak amplitude of the synthetic inversion across the studied region.

and should result in a better estimate of both the local isotropic and anisotropic phase speeds, especially where off-great-circle propagation is important.

Second, uncertainties in local phase speeds can be estimated with eikonal tomography. Instead of minimizing a penalty functional that usually includes some combination of global misfit and model norm or roughness constraints, eikonal tomography directly estimates local phase speed from independent measurements based on different phase traveltime surfaces. Therefore, the uncertainties of the resulting local phase speeds can be determined statistically in a straightforward way. The uncertainties are important for

later 3-D inversion and quantitative comparisons between different models.

Third, eikonal tomography is free from explicit model regularization. The method, therefore, eliminates the need to make *ad hoc* choices of the damping and regularization parameters that are sometimes controversial and may result in dubious models. This particularly is a problem for studies of surface wave azimuthal anisotropy because the increased number of degrees of freedom is often not offset by a comparable improvement in misfit. Eikonal tomography with the additional smoothing intrinsically embedded in the phase front tracking process has no explicit regularization
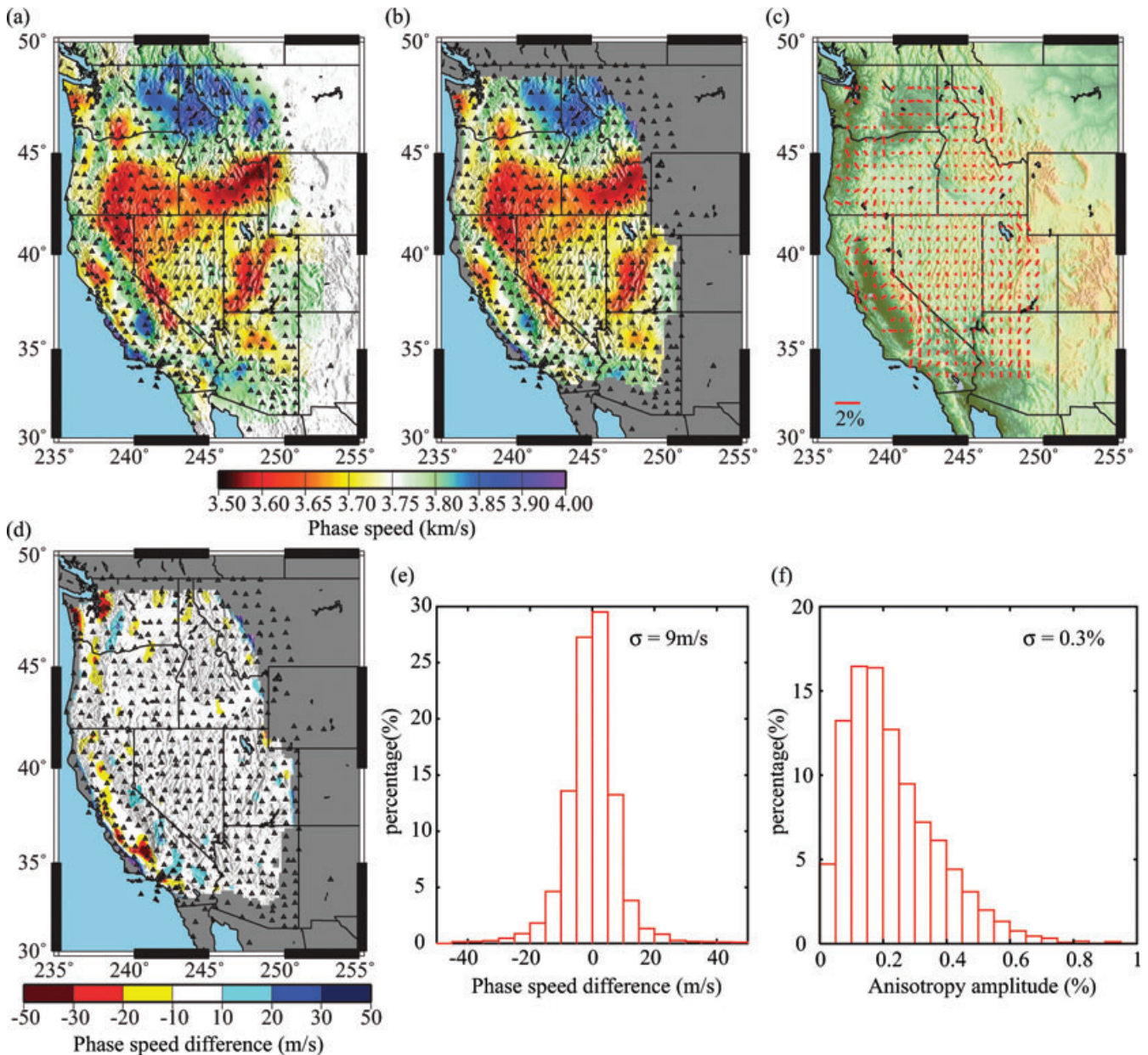
Figure 20. Same as Fig. 19, but for the 36 s simulations.

and the subjectivity of the inverter to affect the tomographic result is restricted.

Fourth, the azimuthal dependence of phase speeds can be measured directly without assuming its parametric form. Unlike classic studies of Pn azimuthal anisotropy (e.g. Morris *et al.* 1969) where the wave speed variation with the direction of propagation is observed directly, traditional surface wave tomography typically posits the relationship between phase speed and the direction of wave propagation based on theoretical studies of weakly anisotropic media (e.g. Smith & Dahlen 1973). The ability to measure and observe the azimuthal dependence of phase speeds directly leads to greater confidence in the information about anisotropy.

There are several limitations on eikonal tomography worthy of note. First, unlike traditional inversion methods where the resolution is controlled by path or kernel densities, eikonal tomography estimates the coherence length of the measurements that is con-

trolled by station spacing. Without applying a more sophisticated traveltime surface interpolation method, this prohibits the use of this technique to resolve structures smaller than the inter-station spacing.

Second, when long period or more complicated surface waves are considered, the second term in eq. (2) can have values more similar to the magnitude of the phase speed anomalies that we seek to resolve. Although our simulations show that the amplitude term is relatively unimportant for our data set, other theoretical and numerical studies, such as Wielandt (1993) and Friederich *et al.* (2000), suggest that when either the velocity anomaly is smaller than a wavelength or the incoming wave is complicated by multipathing, neglect of the amplitude term by the eikonal equation can blur the velocity anomaly and cause systematic errors in the phase speed measurements. It is possible to solve this problem by inverting both phase and amplitude together, which amounts to

recasting the problem in terms of the Helmholtz equation. Amplitude measurements are, however, less accurate than phase measurements and the second spatial derivative of the amplitude variation tends to be unstable and is underestimated, particularly when the station spacing is sparse. The situation is even worse for measurements based on ambient noise cross-correlations where amplitudes have been separately normalized for different stations, so that meaningful amplitude information has been lost. Amplitude anomalies then mainly reflect the distribution of ambient noise sources not structural gradients.

Third, traveltime interpolation schemes usually are unreliable near the periphery of the station coverage that results in increasing both random and systematic errors. Hence, the area that can be imaged by the eikonal tomography method is generally smaller than when a traditional tomography method is applied (Figs 9 and 10). It requires a large-scale array, such as the TA, to really take the advantages of the eikonal tomography method where both applicable areas can be extended and measurement uncertainties can be significantly reduced when ambient noise method is applied.

5.3 Applicability to earthquake tomography

To construct the phase traveltime surfaces in this study we use measurements of ambient noise. In principle, however, eikonal tomography can be applied to phase traveltime measurements based on earthquake waveforms. There are a few differences, however, considering the nature of earthquake measurements.

First, surface waves emitted by a distant source usually develop a certain amount of multipathing that can potentially invalidate the assumption of smoothly varying amplitudes. In fact, this is the fundamental concept of the two plane wave inversion method (e.g. Yang & Forsyth 2006). Friederich *et al.* (2000) showed numerically how wave complexity can contribute to uncertainties in the local phase speeds inferred from the eikonal equation. This problem is relatively minor for measurements based on ambient noise cross-correlations in the western USA because the effective sources (i.e. the stations in the ambient noise method) usually are relatively close, with average distances near 700 km. Other than at the short period end of our study and near regions with sharp velocity contrasts, this is usually too short for multipathing to be well developed. Second, surface wave studies based on teleseismic events usually focus on longer periods (>25 s) due to the strong scattering and attenuation of shorter period signals. At longer periods, when a wavelength is larger than the size of a velocity anomaly, the second term in eq. (2) can blur and distort the velocity anomaly that we wish to resolve (Friederich *et al.* 2000).

Considering these factors, the amplitude term may play a bigger role in eikonal tomography based on earthquake measurements and the second term in eq. (2) should probably be properly taken into account. Unlike ambient noise cross-correlation measurements where only the phase information is retained, the amplitude of the surface wave emitted by an earthquake can be used in the inversion as well. By including amplitude information, the Helmholtz equation can be applied instead of the eikonal equation, and may resolve the local phase velocity structure with greater certainty (Wielandt 1993; Friederich *et al.* 2000; Pollitz 2008).

6 CONCLUSIONS

We present a new method of surface wave tomography called eikonal tomography and argue that this method presents an improvement over traditional methods of ambient noise tomography, particularly as the method is applied to data from the TA component of EarthScope/USArray. The method initiates by tracking phase fronts across the array to produce phase traveltime maps centred on each station, considered as an 'effective source'. The method culminates by interpreting the local gradients of the phase time surfaces in terms of local phase speed and the direction of propagation of the wave.

The most significant advantages of eikonal tomography compared to traditional straight-ray tomography are its more accurate representation of wave propagation, its ability to produce meaningful uncertainty information about the inferred phase speed maps and its production of more reliable information about azimuthal anisotropy. Improvements in the isotropic dispersion maps result predominantly from the method's ability to track the direction of propagation of waves, which is tantamount to use of off-great-circle geometrical rays but without the need for iteration. Improvements in information about azimuthal anisotropy derive from the method's freedom from *ad hoc* choices in regularization. This provides more reliable information about the amplitude of anisotropy, in particular. In addition, the method provides a local visualization of how phase speeds vary with azimuth, which we believe adds considerably to confidence in the results.

Eikonal tomography is an approximate method. It accurately tracks the direction of wave propagation but only approximately incorporates what may be traditionally thought of as finite-frequency effects and assumes a single wave propagating at each point in space. To improve the ability to resolve small-scale feature and reduce systematic errors, future work will focus on finding more sophisticated interpolation schemes as well as incorporating the amplitude term of eq. (2).

REFERENCES

Alsina, D., Snieder, R. & Maupin, V., 1993. A test of the great circle approximation in the analysis of surface waves, *Geophys. Res. Lett.,* **20,** 915–918.

Barmin, M.P., Ritzwoller, M.H. & Levshin, A.L., 2001. A fast and reliable method for surface wave tomography, *Pure appl. Geophys.,* **158,** 1351–1375.

Bensen, G.D. *et al.*, 2007. Processing seismic ambient noise data to obtain reliable broad-band surface wave dispersion measurements, *Geophys. J. Int.,* **169,** 1239–1260.

Bensen, G.D., Ritzwoller, M.H. & Shapiro, N.M., 2008. Broad-band ambient noise surface wave tomography across the United Stated, *J. geophys. Res.,* **113,** B05306, 21 pages, doi: 10.1029/2007JB005248.

Bodin, T. & Maupin, V., 2008. Resolution potential of surface wave phase velocity measurements at small arrays, *Geophys. J. Int.,* **172,** 698–706.

Boschi, L., 2006. Global multiresolution models of surface wave propagation: comparing equivalently regularized Born and ray theoretical solutions, *Geophys. J. Int.,* **167,** 238–252.

Brisbourne, A.M. & Stuart, G.W., 1998. Shear-wave velocity structure beneath North Island, New Zealand, from Rayleigh-wave interstation phase velocities, *Geophys. J. Int.,* **133,** 175–184.

Dahlen, F.A., Hung, S.-H. & Nolet, G., 2000. Fre′chet kernels for finite-frequency travel times, I: theory, *Geophys. J. Int.,* **141,** 157–174.

Deschamps, F., Lebedev, S., Meier, T. & Trampert, J., 2008. Azimuthal anisotropy of Rayleigh-wave phase velocities in the east-central United States, *Geophys. J. Int.,* **173,** 827–843.

Ekstrom, G., Tromp, J. & Larson, E.W.F., 1997. Measurements and global models of surface wave propagation, *J. geophys. Res,* **102,** 8137–8157.

Friederich, W., 1998. Wave-theoretical inversion of teleseismic surface waves in a regional network: phase-velocity maps and a three-dimensional upper-mantle shear-wave-velocity model for southern Germany, *Geophys. J. Int.,* **132,** 203–225.

Friederich, W., Hunzinger, S. & Wielandt, E., 2000. A note on the interpretation of seismic surface waves over three-dimensional structures, *Geophys. J. Int.,* **143,** 335–339.

Laske, G. & Masters, G., 1998. Surface-wave polarization data and global anisotropic structure, *Geophys. J. Int.,* **132,** 508–520.

Levshin, A.L., Ritzwoller, M.H., Barmin, M.P., Villaseñor, A. & Padgett, C.A., 2001. New constraints on the arctic crust an uppermost mantle: surface wave group velocities *Pn* and *Sn, Phys. Earth planet. Inter.,* **123,** 185–204.

Levshin, A.L., Barmin, M.P., Ritzwoller, M.H. & Trampert, J., 2005. Minor-arc and major-arc global surface wave diffraction tomography, *Phys. Earth planet. Inter.,* **149,** 205–223.

Lin, F.C., Moschetti, M.P. & Ritzwoller, M.H., 2008. Surface wave tomography of the western United States from ambient seismic noise: Rayleigh and Love wave phase velocity maps, *Geophys. J. Int.,* **173,** 281–298.

Lin, F.C, Ritzwoller, M.H., Townend, J., Savage, M. & Bannister, S., 2007, Ambient noise Rayleigh wave tomography of New Zealand, *Geophys. J. Int.,* **170,** 649–666.

Montelli, R., Nolet, G. & Dahlen, F.A., 2006. Comment on 'Banana-doughnut kernels and mantle tomography' by van der Hilst and de Hoop, *Geophys. J. Int.,* **167,** 1204–1210.

Morris, G.B., Raitt, R.W. & Shor, G.G., 1969. Velocity anisotropy and delay-time maps of Mantle near Hawaii, *J. geophys. Res,* **74,** 4300–4316.

Moschetti, M.P., Ritzwoller, M.H. & Shapiro, N.M., 2007. Surface wave tomography of the western United States from ambient seismic noise: Rayleigh wave group velocity maps, *Geochem., Geophys., Geosys.,* **8,** Q08010, doi: 10.1029/2007GC001655.

Nolet, G., 1990. Partitioned wave-form inversion and 2D structure under the NARS array, *J. geophys. Res.,* **95,** 8513–8526.

Pollitz, F.F., 2008. Observations and interpretation of fundamental-mode Rayleigh wavefields recorded by the Transportable Array (USArray), *J. geophys. Res.,* **113,** B10311.

Prindle, K. & Tanimoto, T., 2006. Teleseismic surface wave study for S-wave velocity structure under an array: Southern California, *Geophys. J. Int.,* **166,** 601–621.

Ritzwoller, M.H. & Levshin, A.L., 1998. Eurasian surface wave tomography: group velocities, *J. geophys. Res.,* **103,** 4839–4878.

Ritzwoller, M.H., Shapiro, N.M., Barmin, M.P. & Levshin, A.L., 2002. Global surface wave diffraction tomography, *J. geophys. Res.,* **107,** 2335–2347.

Roth, M., Muller, G. & Snieder, R., 1993, Velocity shift in random media, *Geophys. J. Int.,* **115,** 552–563.

Sabra, K.G., Gerstoft, P., Roux, P. & Kuperman, W.A., 2005. Surface wave tomography from microseisms in Southern California, *Geophys. Res. Lett.,* **32,** L14311, doi: 10.1029/2005GL023155.

Shapiro, N.M., Campillo, M., Stehly, L. & Ritzwoller, M.H., 2005. High resolution surface wave tomography from ambient seismic noise, *Science,* **307**(5715), 1615–1618.

Shearer, P., 1999. *Introduction to Seismology,* Cambridge University Press, Cambridge.

Smith, M.L. & Dahlen, F.A., 1973. Azimuthal dependence of Love and Rayleigh-wave propagation in a slightly anisotropic medium, *J. geophys. Res.,* **78,** 3321–3333.

Smith, W.H.F. & Wessel, P., 1990. Gridding with continuous curvature splines in tension, *Geophysics,* **55,** 293–305.

Smith, D.B., Ritzwoller, M.H. & Shapiro, N.M., 2004. Stratification of anisotropy in the Pacific upper mantle, *J. geophys. Res.,* **109,** B11309, doi: 10.1029/2004JB003200.

Trampert, J. & Spetzler, J., 2006. Surface wave tomography: finite frequency effects lost in the null space, *Geophys. J. Int.,* **164,** 394–400.

Trampert, J. & Woodhouse, J.H., 1996. High resolution global phase velocity distributions, *Geophys. Res. Lett.,* **23,** 21–24.

Trampert, J. & Woodhouse, J.H., 2003. Global anisotropic phase velocity maps for fundamental mode surface waves between 40 and 150 s, *Geophys. J. Int.,* **154,** 154–165.

Tromp, J., Tape, C. & Liu, Q.Y., 2005. Seismic tomography, adjoint methods, time reversal and banana-doughnut kernels, *Geophys. J. Int.,* **160,** 195–216.

Van Der Hilst, R.D. & de Hoop, M.V., 2005. Banana-doughnut kernels and mantle tomography, *Geophys. J. Int.,* **163,** 956–961.

Van Der Lee, S. & Frederiksen, A., 2005. Surface wave tomography applied to the North American upper mantle, in *Seismic Earth: Array Analysis of Broadband Seismograms,* pp. 67–80, eds Levander A. & Nolet G., American Geophysical Union Monograph, American Geophysical Union. Washington, D.C.

Wielandt, E., 1993. Propagation and structural interpretation of nonplane waves, *Geophys. J. Int.,* **113,** 45–53.

Woodhouse, J.H. & Dziewonski, A.M., 1984. Mapping the upper mantle—3-dimensional modeling of earth structure by inversion of seismic waveforms, *J. geophys. Res.,* **89,** 5953–5986.

Yang, Y. & Forsyth, D.W., 2006. Rayleigh wave phase velocities, small-scale convection, and azimuthal anisotropy beneath southern California, *J. geophys. Res.,* **111,** B07306.

Yang, Y., Ritzwoller, M.H., Levshin, A.L. & Shapiro, N.M., 2007. Ambient noise Rayleigh wave tomography across Europe, *Geophys. J. Int.,* **168**(1), 259–274.

Yang, Y., Ritzwoller, M.H., Lin, F.-C., Moschetti, M.P. & Shapiro, N.M., The structure of the crust and uppermost mantle beneath the western US revealed by ambient noise and earthquake tomography, *J. geophys. Res.*, **113,** B12310, doi:10.1029/2008JB005833.

Yao, H.J., Van Der Hilst, R.D. & de Hoop, M.V., 2006. Surface-wave array tomography in SE Tibet from ambient seismic noise and two-station analysis: I. Phase velocity maps, *Geophys. J. Int.,* **166,** 732–744.

Yoshizawa, K. & Kennett, B.L.N., 2002. Determination of the influence zone for surface wave paths, *Geophys. J. Int.,* **149,** 441–454.

Zhou, Y., Dahlen, F.A. & Nolet, G., 2004. Three-dimensional sensitivity kernels for surface wave observables, *Geophys. J. Int.,* **158,** 142–168.

Zhou, Y., Nolet, G., Dahlen, F.A. & Laske, G., 2005. Finite-frequency effects in global surface-wave tomography, *Geophys. J. Int.,* **163,** 1087–1111.